UNIVERSIDADE DE LISBOA
FACULDADE DE CIÊNCIAS
DEPARTAMENTO DE FÍSICA

Antiproton production in proton on helium collisions at the AMBER Experiment

Guilherme Filipe Marques Almeida

Mestrado em Engenharia Física

Dissertação orientada por:
Catarina Marques Quintans
Jorge Miguel de Brito Almeida Sampaio

2025

Resumo

Nesta tese, os dados recolhidos na experiência *Apparatus for Meson and Baryon Experimental Research* (AMBER), localizada no CERN, são utilizados para medir a razão entre secções eficazes diferenciais de produção de hadrões carregados, tais como piões, kaões, protões e antiprotões. Observações cosmológicas, por exemplo da velocidade de afastamento das galáxias no universo, há muito que apontam para a existência de um tipo de matéria até agora desconhecido, a chamada Matéria Escura. Estima-se que apenas 5% de toda a matéria do universo seja bariónica, sendo 26% matéria escura e 69% energia escura. Com base na hipótese de que a Matéria Escura é composta por partículas massivas que decaem para ou que interagem com matéria do modelo padrão por via da força fraca, conhecidas por *WIMP*. A medida de um excesso de antimatéria nos fluxos de raios cósmicos, quando comparado à quantidade esperada a partir de fontes físicas «comuns», constituíria uma evidência indireta da existência de Matéria Escura. Tais fluxos são medidos em experiências como *Alpha Magnetic Spectrometer*, localizada na órbita espacial da Terra, na Estação Espacial Internacional. No entanto, a interpretação desses resultados depende de um conhecimento muito preciso da produção de antimatéria em colisões protão-protão, protão-hélio e protão-deutério (as colisões mais frequentes que ocorrem no espaço interestelar), ou seja da taxa esperada de produção de antimatéria, nomeadamente antiprotões.

A experiência AMBER é uma experiência de alvo fixo localizada no SPS do CERN, na qual um feixe de protões atinge um alvo fixo de hélio líquido a alta pressão. Um feixe primário de protões fornecido pelo SPS, com momento de 400 GeV/c, atinge um alvo de berílio, produzindo um feixe secundário de hadrões ou muões carregados, que podem ser seleccionados por carga eléctrica e num intervalo de momento de 60 a 250 GeV/c, usando conjuntos de dipolos e quadrupolos que constituem a complexa ótica de feixe da linha M2. Uma vez que o feixe produzido é uma mistura de hadrões (protões, piões e kaões), a linha de feixe possui dois detetores CEDAR, que utilizam o princípio de Cherenkov na identificação das partículas. A 190 GeV/c espera-se uma fração aproximada de 75% de protões, 24% de piões positivos e 1% de kaões positivos. Os dados analisados nesta tese foram recolhidos por AMBER durante o período W01 pertencente ao Run de 2023, à energia de 190 GeV/c. Foi realizada posteriormente a calibração em energia e em tempo de cada um dos detetores, assim como o alinhamento *offline* dos detetores entre si. O espetrómetro de AMBER inclui diferentes tipos de detetores de traçamento e de identificação de partículas, num total de mais de 300 planos. Dois ímans dipolares garantem grande aceitância angular (até 200 mrad) e em momento (5-190 GeV/c). A reconstrução das trajetórias das partículas de saída e dos vértices de interação a partir dos sinais dos detetores foi realizada no *software* CORAL; os dados foram armazenados em ficheiros *ROOT* chamados *mini Data Summary Trees* (mDST). Utilizou-se o programa *PHysics Analysis Software Tool* (PHAST) para processar os dados contidos nas mDSTs, guardando a informação relevante para o estudo em questão em ficheiros *ROOT*. Durante o processo de análise, foram determinados novos critérios de seleção para filtrar os dados, com o objetivo de melhorar o tamanho da amostra e garantir uma boa reconstrução da física subjacente aos processos em estudo; esta seleção foi aplicada tanto às trajetórias das partículas quanto aos seus vértices.

O trabalho desenvolvido nesta tese focou-se sobretudo na identificação dos problemas relacionados com a estabilidade do espetrómetro e na otimização dos cortes que garantem a boa qualidade dos eventos. Detetou-se a não-sincronização dos detetores Pixel MicroMega relativamente aos restantes, problema a ser resolvido posteriormente. Foi feita uma identificação rigorosa da região do alvo iluminada pelo feixe, fator muito importante para uma correta avaliação da secção eficaz absoluta.

Uma simulação de Monte Carlo (MC) foi utilizada para calcular as correções de aceitância, que incluem a aceitância geométrica e as eficiências de reconstrução e dos detetores, e para determinar a resolução do espectrómetro, a fim de escolher a largura dos bins dos histogramas de momento total, momento transverso e as posições (X,Y) e Z para os vértices primários. A simulação foi realizada em três etapas: primeiro, os eventos físicos do tipo "Soft QCD" foram gerados usando o programa PYTHIA 8; segundo, o dispositivo experimental de AMBER foi simulado utilizando o software TGEANT que reproduz especificamente a experiência AMBER e faz o transporte das partículas, gerando as interações com os detectores, baseado em GEANT4; terceiro, os dados de MC foram reconstruídos pelo programa CORAL e guardados em árvores *ROOT* semelhantes às utilizadas para os dados reais.

Os dados gerados e reconstruídos foram analisados a partir do programa PHAST, e guardados em árvores *ROOT* distintas. As respostas dos detetores CEDAR e RICH não foram simuladas, portanto a identificação dos traços das partículas reconstruídas foi feita por associação da partícula reconstruída com a sua contraparte gerada. O ficheiro de feixe usado na simulação foi produzido previamente por especialistas, a partir dos dados reais.

De todos os eventos produzidos, nem todos são detetáveis pelo espetrómetro, seja devido à dimensão dos detetores, às suas zonas mortas, ou a ineficiências. A chamada aceitância geométrica da experiência é calculada com recurso ao Monte Carlo, como a razão entre os eventos reconstruídos e gerados. A aceitância é obtida em três dimensões: a posição Z do vértice, o momento e o momento transverso dos hadrões produzidos. Embora muito semelhante entre partículas e antipartículas, não é exactamente igual para as duas cargas, e uma das razões é que a segunda parte do espectrómetro (SAS) não é simétrica em relação à linha de feixe, estando desviada por forma a acompanhar a curvatura do feixe no campo dipolar dos ímans SM1 e SM2.

A eficiência da identificação de partículas realizada pelo detetor RICH e a probabilidade de erro nessa identificação foram tidas em conta na obtenção das contagens reais de partículas em cada bin, através de um processo chamado RICH *unfolding*. A matriz do RICH unfolding foi produzida anteriormente por especialistas e aplicada aos histogramas de dados reais evento-a-evento em conjunto com a correção de aceitância.

Por fim, a secção eficaz bi-dimensional foi calculada em unidades arbitrárias para cada hadrão (uma vez que a correção de luminosidade não foi aplicada), em bins de (P_T, P). O cálculo da razão das secções eficazes de produção entre as duas cargas de cada hadrão, π^-/π^+, K^-/K^+ e $\bar{p}/p$, foi obtido para o mesmo binning, contabilizando apenas os erros estatísticos. A razão entre seções eficazes de particula e respectiva antipartícula é um observável com algumas vantagens relativamente às seções eficazes absolutas: não requer o conhecimento da luminosidade (que cancela na razão), e a sua medida tende a ter menores erros sistemáticos, uma vez que parte dos sistemáticos experimentais também cancela na razão.

Os resultados obtidos nesta tese são preliminares, visto que uma das conclusões obtidas é que o Monte Carlo utilizado não reproduz suficientemente bem os dados reais e alguns problemas na calibração temporal dos detetores foram identificados. Por outro lado, é natural que uma nova produção que inclua esses melhoramentos irá requerer nova avaliação da matriz de unfolding de PID do RICH. Finalmente, só a análise dos dados tomados às diferentes energias permitirá aceder com a precisão requerida

à dependência da produção de antimatéria com a energia.

Palavras chave: matéria escura, produção de antimatéria, experiência de alvo fixo, AMBER, antiprotões

Abstract

In this thesis, data collected in the CERN AMBER is used to measure the differential cross-section ratios for hadrons such as pions, kaons, and protons/antiprotons. This study is based on the premise that Dark Matter is massive and can decay into or interact with standard model matter via the weak force (WIMPs). Thus, measuring an excess of antimatter particle fluxes, with respect to that expected from "common" physics sources, would provide indirect evidence for Dark Matter. Such fluxes are measured in Earth orbit experiments like AMS. The results' interpretation relies on the precise knowledge of namely proton on helium collisions, one of the most frequent sources of antimatter occurring in the interstellar space.

AMBER is a fixed target experiment using a proton beam of 190 GeV. Data was taken during the period W01 of the 2023 Run. During the analysis of this data new selection criteria for filtering hadrons were used, to improve the sample quality and size.

A Monte Carlo (MC) simulation was used to calculate the acceptance of the AMBER experiment. The MC simulation was also used to aid in the decision of the cross-section binning in momentum and transverse momentum of the produced hadrons, and the (X,Y) and Z position of their primary vertices.

To account for errors in the particle identification process performed by the RICH detector and obtain the true particle counts for each bin, a procedure was performed that consists in applying the inverse of a matrix with the probability of true identification, as well as the probability of mis-identifications for each hadron type considered, called RICH unfolding.

Cross-sections were calculated in arbitrary units for each hadron, since luminosity correction was not applied. The computation of the cross-section ratios between the two charges of a given hadron type were obtained.

Keywords: dark matter search, antimatter production, fixed target experiment, AMBER, antiprotons

Acknowledgments

I want to express my gratitude to everyone who has supported me throughout this process. A special thanks to Catarina Quintans, who invited me to the AMBER subgroup in 2021 after my summer internship and has been guiding me ever since, particularly during the completion of this thesis. I also want to express my gratitude to Davide Giordano, whose work served as the launchpad for my thesis and who spent his time helping me on many occasions. I also want to thank Professor Jorge Sampaio and my colleague Barbara Pereira. I want to thank my parents, Graça and Paulo, and my sister, Margarida. I want to thank Patrícia who supported me mentally throughout this last year.

Contents

List of Figures **xiii**

List of Tables **xvii**

List of Abbreviations **xix**

1 Introduction **1**

2 Experimental Setup **3**
2.1 Beam line . . . 3
2.2 Beam composition . . . 3
2.3 Beam reconstruction . . . 5
2.3.1 Beam Telescope . . . 5
2.4 Target . . . 5
2.5 Trigger . . . 6
2.6 Spectrometer . . . 7
2.6.1 RICH . . . 9
2.6.2 Scintillating Fibers in the Spectrometer . . . 9
2.6.3 Micro-Mesh Gaseous Structure . . . 9
2.6.4 Drift Chambers . . . 9
2.6.5 DAQ . . . 10
2.6.6 DCS . . . 10

3 Data Analysis **13**
3.1 Event selection . . . 13
3.2 Tracks selection . . . 20

4 Monte Carlo Analysis **25**
4.1 Generated data . . . 25
4.1.1 MC truth event and track selection . . . 25
4.2 Reconstructed MC data . . . 26
4.2.1 Event and track selection . . . 26
4.3 MC/RD comparisons . . . 26
4.3.1 Momentum . . . 27
4.3.2 Transverse momentum . . . 27
4.3.3 X, Y, Z vertex position . . . 28
4.4 Acceptance Corrections . . . 29

4.4.1 Bin studies . . . 29
4.4.1.1 Z_{vtx} . . . 29
4.4.1.2 Momentum . . . 30
4.4.1.3 Transverse Momentum . . . 31
4.4.2 Acceptance Corrections . . . 31
4.4.2.1 Pions . . . 32
4.4.2.2 Kaons . . . 34
4.4.2.3 Protons . . . 36

5 Cross-section ratios **39**
5.1 RICH-1 unfolding . . . 39
5.1.1 Pions . . . 40
5.1.2 Kaons . . . 41
5.1.3 Protons . . . 42
5.2 Cross-section ratios . . . 44

6 Conclusions **47**

List of Figures

1.1 Relative contributions of production channels to the secondary antiproton source spectrum as a function of the kinetic energy of the antiprotons. Taken from [2]. 2
1.2 Left: present AMS $\bar{p}$ experimental errors (black) at 10 and 200 GeV, and the cross-section (red) and propagation (blue) uncertainties from theory. Right: expected evolution of these errors in the near future and how these uncertainties might reach levels comparable to AMS data. Taken from [6]. 2

2.1 Beam composition versus beam momentum (GeV/c). 4
2.2 CEDAR schematics, taken from [9]. We can observe in blue the lens used to focus the radiation emitted from the light cone, in green we have the characteristic proton light cone that can pass trough the diaphragm, and in red, the light coming from another particle that cannot pass. 4
2.3 Target schematics, including the COMPASS target solenoid/dipole and the dilution refrigerator systems, that in 2023 were not used, remaining as passive. The dilution refrigerator was not used during this data taking. 6
2.4 COMPASS 2022 experimental setup layout. 8
2.5 Schematics of RICH detector. 9
2.6 Schematics of a Drift Chamber detector. Taken from [7]. 10
2.7 Graphical User Interface of the DCS. 11

3.1 Analysis Workflow 13
3.2 Distribution of time in spill for events. The red lines show the upper and lower limits of the cut. 14
3.3 (a): Distribution of ΔZ in cm fitted with a sum of a Gaussian function and a second-order polynomial function; (b): Distribution of Z vertex for both Real Data and Monte Carlo simulations. 15
3.4 Distributions of X (top) and Y (bottom) positions for primary vertices 16
3.5 Distribution of number of hits in Silicon detectors (top) and in Scintillating fiber detectors (bottom). 17
3.6 Distributions of the beam track X and Y positions at target entry and exit. 18
3.7 Distribution of number of hits in the CEDAR's PMTs. 19
3.8 Distribution of the number of outgoing particles from each vertex. 19
3.9 χ^2/ndf of the tracks selected. This reduced χ^2 is computed from the distance to track of the detector hits that were associated to the given track. 20
3.10 Distributions of Z_{first} (top) and Z_{last} (bottom). The red line is placed at $Z = 350$ cm. . . . 21
3.11 Distribution of the tracks' X/X_0 in the spectrometer. 21

3.12 Distribution of the timing of the outgoing tracks. 22
3.13 Distributions of the timing of the outgoing tracks according to their respective Z_{first}. . . 22
3.14 Angle of the Cherenkov photons emitted vs Momentum of the crossing particle at RICH entrance. Particle identification was performed using likelihoods from the PHAST PaPid class. 23
3.15 Momentum of selected hadron tracks at RICH entrance, before cutting on non-extrapolated to RICH ones. 24
3.16 Polar angles of the hadron tracks extrapolated to RICH. 24

4.1 Comparison between MC reconstructed data and real data as a function of momentum. The top row shows the comparison of the two, and the bottom row shows their ratio RD/MC. 27
4.2 Comparison between MC reconstructed data and real data as a function of transverse momentum. The top row shows the comparison, and the bottom row shows the ratio between the two. 28
4.3 Comparison between MC reconstructed data and real data for X, Y, and Z. The top row shows the comparison, and the bottom row shows the ratio between the two. 29
4.4 Distribution of Z_{vtx}. Red lines indicate the different bins. Real data. 30
4.5 Distribution of momentum at the primary vertex for different hadrons. Real data. 30
4.6 Distribution of transverse momentum for different hadrons. Real data. 31
4.7 Distributions of the **acceptance relative error** for the different Z_{vtx} bins for **pions** as a function of momentum in bins of transverse momentum. The two different charges are also plotted together. 33
4.8 **Acceptance** corrections for **pions** as a function of momentum in bins of transverse momentum and Z_{vtx}. 34
4.9 Distributions of **acceptance relative error** for the different Z_{vtx} bins for **kaons** as a function of momentum in bins of transverse momentum. The two different charges are also plotted together. 35
4.10 **Acceptance** corrections for **kaons** as a function of momentum in bins of transverse momentum and Z_{vtx}. 36
4.11 Distributions of **acceptance relative error** for the different Z_{vtx} bins for **protons** and **antiprotons** as a function of momentum in bins of transverse momentum. The two different charges are also plotted together. 37
4.12 **Acceptance** corrections for **protons** and **antiprotons** as a function of momentum in bins of transverse momentum and Z_{vtx}. 38

5.1 Spectra for pions with acceptance and RICH unfolding applied. 41
5.2 Spectra for kaons with acceptance and RICH unfolding applied. 42
5.3 Spectra for protons/antiprotons with acceptance and RICH unfolding applied. 43
5.4 Cross-section ratios for pions as a function of momentum. Each pad represents a bin of transverse momentum. 44
5.5 Cross-section ratios for kaons as a function of momentum. Each pad represents a bin os transverse momentum. 45

5.6 Cross-section ratios for antiprotons/protons as a function of momentum. Each pad represents a bin os transverse momentum. Bins that were previously rejected are shaded in gray. 45

List of Tables

2.1 2023 AMBER data taking. 3

3.1 Event selection criteria 20
3.2 Tracks selection criteria of the tracks that passed vertex selection. 24

List of Abbreviations

AMBER Apparatus for Meson and Baryon Experimental Research.. iii–v, vii, xvii, 1, 3, 5, 13, 25, 47

CEDAR Cherenkov Detectors with Achromatic Ring.. iii, iv, xiii, 4, 5, 18, 19, 25

CERN Conseil Européen pour la Recherche Nucléaire.. iii, vii, 1, 2, 47

COMPASS COmmon Muon Proton Apparatus for Structure and Spectroscopy.. xiii, 3, 5, 7, 8, 13, 23, 25

CORAL COmpass Reconstruction AnaLysis software package.. iii, iv, 13

CR Cosmic Ray.. 1

DAQ Data AcQuisition.. 6, 25

DC Drift Chamber.. 9

DM Dark Matter.. 1

ISM InterStellar Medium.. 1

ISS International Space Station.. 1

LAS Large Angle Spectrometer.. 7, 9

MC Monte Carlo.. iv, vii, xi, xiv, 14, 15, 25–29, 31

mDST mini Data Summary Trees.. iii, 13

MP Micro-Mesh Gaseous Structure.. 22, 47

PHAST PHysics Analysis Software Tool.. iii, iv, xiv, 13, 23, 25

PID Particle Identification.. iv, 24, 25, 40

RD Real Data.. 14, 15, 27–29

RICH Ring-imaging Cherenkov.. iv, vii, xi–xiv, 9, 23–25, 30–32, 34, 36, 39–43, 47

SAS Small Angle Spectrometer.. 7

SciFi Scintillating Fibers.. 5, 6, 9, 16

List of Abbreviations

SPS Super Proton Synchrotron.. iii, 3

TGEANT Total Geometry And Tracking.. iv, 25

VSAT Very Small Area Tracker. 9

WIMP Weakly Interacting Massive Particle.. iii, 1

Chapter 1

Introduction

A convergence of empirical evidence indicates that the dominant matter component of the universe is non-baryonic and devoid of electric charge. Because it does not interact with light, it cannot be seen directly. This unknown component is commonly referred to as dark matter (DM). The most appealing hypothesis is that DM consists of weakly interacting massive particles (WIMPs), which are predicted to annihilate into or interact with standard-model particles. If this hypothesis proves to be correct, then we should be able to detect such particles. The percentage of baryonic matter in the universe is only ~ 5, the rest being 68.6 % of Dark Energy and ~ 26 % of Dark Matter [1].

DM may appear as an extra source of multi-messenger cosmic-ray matter (CR) components like antiprotons, positrons, and antideuterons in the data from experiments based in space, like the AMS-02 in the International Space Station (ISS). The antiproton is considered a "golden-probe" and provides advantages such as high statistics, however that will also lead to a high background. Cosmic-ray antiprotons are mainly produced from inelastic scattering in the interstellar medium (ISM), especially of protons with other protons, deuterons, or Helium nuclei at rest. In this indirect search for DM signals, the accurate measurement of antimatter produced by conventional sources is crucial. As illustrated in Figure 1.1 (from [2]), the secondary antiproton spectrum is dominated around 90% by collisions between protons or collisions with Helium, the elements with most significant densities in ISS. These results underline the necessity of precise measurements in the $p+p \rightarrow \bar{p}+X$ and $p+He \rightarrow \bar{p}+X$ channels' cross sections, which currently represent the main source of uncertainty in the calculation of the secondary antiproton flux.

The AMS experiment measured an antiprotons flux in the range 0.5 GeV up to 500 GeV, and will continue operating at the ISS at least until 2030. At the moment, the AMS results are consistent with what is expected if they are of secondary origin, but the present theory uncertainties have some margin for indirect evidence of DM contribution.

Thanks to the versatility of the M2 beamline at CERN, which provides hadron beams in a very wide range of momenta, the AMBER experiment provided data that, once carefully analyzed will lead to very precise measurements of the antiproton production cross sections in proton on helium collisions, see Fig. 2.4.

The measurements were proposed in 2019 and approved by the CERN Research Council in December 2020 [3]. The measurements took place in 2023. A beam energy scan was done, that consisted of six periods of data-taking at proton beam momenta: 60, 80, 100, 120, 160, 190, 250 GeV/c.

The goal of this work is to calculate the differential cross section $\left(\frac{d^2\sigma}{dpd\theta}\right)$ with an uncertainty below 3%, for all proton beam energies.

1. INTRODUCTION

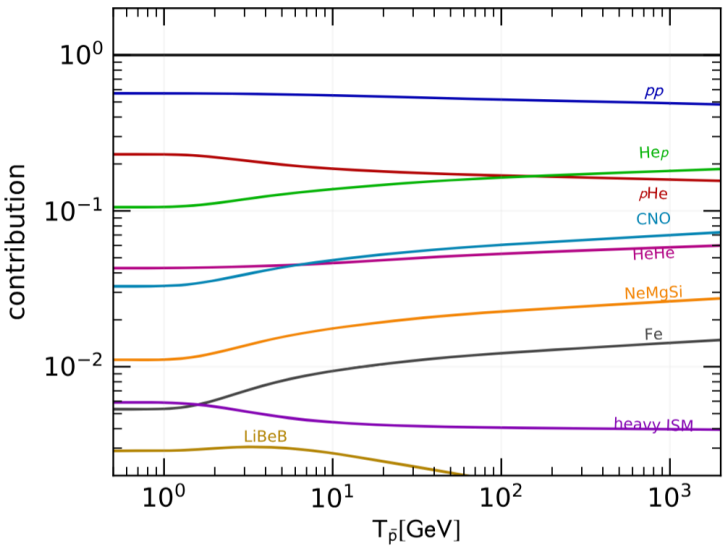

Figure 1.1: Relative contributions of production channels to the secondary antiproton source spectrum as a function of the kinetic energy of the antiprotons. Taken from [2].

Present uncertainties used in the theory models for the prompt antiproton production by common sources are at the level of $\pm$ 8% at 2σ for antiproton kinetic energies $T_{\bar{p}} > 5$ GeV [2] and are inferred mainly from the measurements of proton on Carbon done by NA49 at SPS/CERN [4], and of proton on helium done by LHCb on fixed mode and protons at 6.5 TeV at LHC/CERN [5].

The AMBER already taken data and existing and future LHCb data are expected to improve significantly the theory uncertainties, namely in what concerns the cross-section uncertainties, in the near future. Figure 1.2 illustrates the expected evolution of these errors, together with evolution in the statistical error that may come from the future AMS-upgrade. The theory errors may reach a level close to the experimental AMS fluxes error, as shown in figure 1.2 [6].

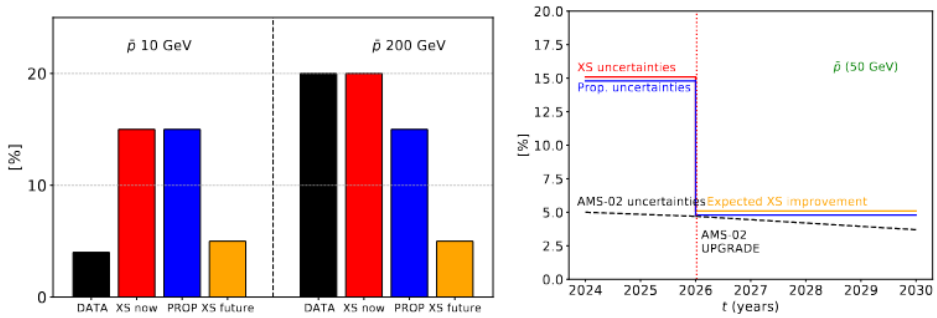

Figure 1.2: Left: present AMS $\bar{p}$ experimental errors (black) at 10 and 200 GeV, and the cross-section (red) and propagation (blue) uncertainties from theory. Right: expected evolution of these errors in the near future and how these uncertainties might reach levels comparable to AMS data. Taken from [6].

Chapter 2

Experimental Setup

The AMBER 2023 experimental setup is based on the COMPASS setup [7], with a newly built target. This chapter will be devoted to describing the beam, target, and spectrometer of AMBER.

2.1 Beam line

The beam is provided by the M2 (see figure 2.4) beam line located in Experimental Hall North 2 (EHN2), which is produced by a primary beam of protons at 400 GeV extracted from the Super Proton Synchrotron (SPS) hitting a primary Beryllium target (T6). The M2 beam line can produce either a secondary hadron beam with a maximum intensity per spill of $\sim 10^9$; or a tertiary muon beam with a maximum intensity of $\sim 3 \times 10^8$ per spill, by inserting or removing a hadron absorber in the beam line. Either beam polarity can be selected, and over a wide range in momenta. This study focused on period W01, specifically on a positive beam with a momentum of 190 GeV/c. Table 2.1 shows the different periods and their corresponding beam energy selected for the data-taking year of 2023, to measure antiproton production from proton on helium collisions.

For this data-taking, the typical beam intensities were $\sim 5 \times 10^5$ particles per spill. The beam arrives at AMBER in packages with a flat intensity, lasting 4.9 s, known as a spill. A spill repeats in a super-cycle of $15 - 40$ s. From all the data periods, W01 was the first to be collected and analyzed. The first study was performed by D. Giordano in [8].

Table 2.1: 2023 AMBER data taking.

Period Name	Beam mom. (GeV/c)	Collision energy $\sqrt{S_{NN}}$ (GeV)	Number of Spills
W01	190	18.9	11000
W02-W03	60	10.7	37000
W04	100	13.8	13700
W05	250	21.7	7300
W06	160	17.3	8500
W07	80	12.3	13400

2.2 Beam composition

The positive hadron beam consists of a mixture of protons, pions, and kaons, in different proportions, depending on the beam momentum. In the M2 beamline, the momentum can be varied in a simple way,

by changing the beam optics formed by many dipoles, quadrupoles and collimators. At 190 GeV/c, protons dominate in the order of 75 %, while at 24 % π^+ is the second largest component, and kaons represent 1.4 %. Figure 2.1 shows the beam composition against momentum [9] .

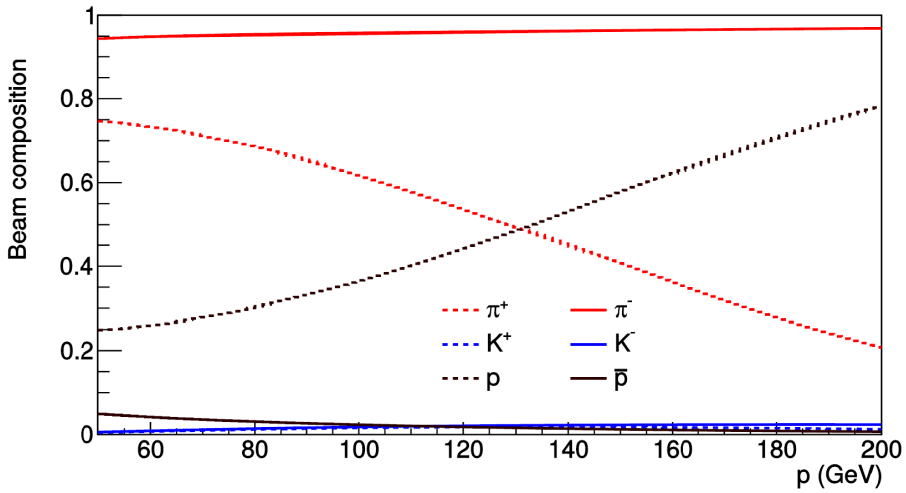

Figure 2.1: Beam composition versus beam momentum (GeV/c).

CEDAR

As previously shown, the positive hadron beam has a different fraction of pions, kaons, and protons; to study $p+He \rightarrow \bar{p}+X$ events, there needs to be a way to identify the beam particle in each event. For this, we use two Cherenkov Detectors with Achromatic Ring (CEDAR). The CEDAR detector uses the Cherenkov effect, a well-known effect where a charged particle, by traversing a medium, emits a light cone known as the Cherenkov photons. These photons are reflected on mirrors and detected in the 8 photomultipliers (PMTs) placed in a circle. There is also a diaphragm that is used to select different radii of Cherenkov rings, which depend on the mass of each particle. More information about this detector can be found in [10]

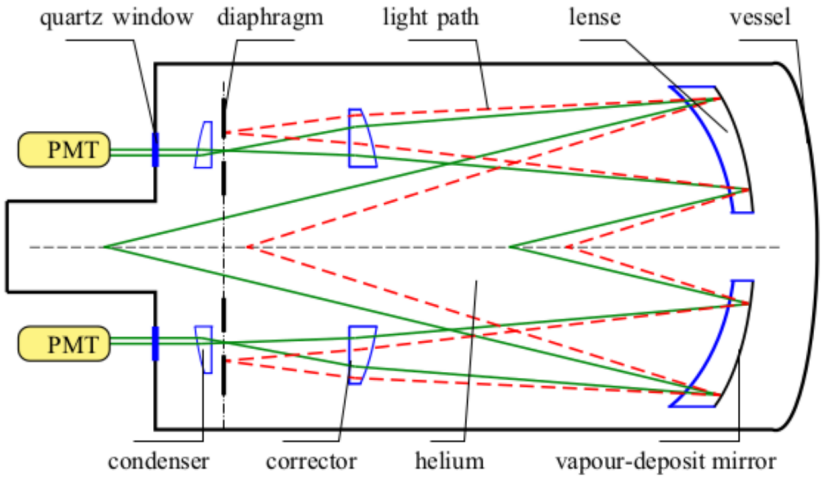

Figure 2.2: CEDAR schematics, taken from [9]. We can observe in blue the lens used to focus the radiation emitted from the light cone, in green we have the characteristic proton light cone that can pass trough the diaphragm, and in red, the light coming from another particle that cannot pass.

The pressure over temperature of the helium gas inside the CEDAR is proportional to its refractive index, $P/T \propto (n-1)$, so by assuming constant temperature and adjusting pressure, it is possible to adjust the diaphragm aperture such that only proton Cherenkov photons pass. However, due to inefficiencies such as optical aberrations, the resolution of the Cherenkov ring is affected, and thus, a minimum number of hits in the PMTs should be required. This minimum number of hits will be discussed further. The CEDARs are located 50 m upstream of the AMBER beam telescope. Figure 2.2 shows the schematics of the CEDAR.

2.3 Beam reconstruction

2.3.1 Beam Telescope

The beam telescope is a set of detectors used to obtain the time and spatial position of the beam tracks, composed of two detector types: the Silicon Microstrip detectors, which have good spatial resolution, and the Scintillating Fiber detectors, which have good time resolution.

- **Silicon Microstrip (Silicon)**

  The silicon microstrip trackers are detectors composed of 2 wafers of silicon sensors with an angle of 5 deg between each other. Each detector has 4 planes: X, Y, U, and V. There are 3 stations placed upstream of the target used for the beam reconstruction. The typical silicon microstrip detector space resolution is $7-11$ μm.

- **Scintillating Fibers (SciFi)**

  In the beam telescope, there are 3 scintillating fiber detector stations: FI01, FI02 with X and Y planes, and FI15 with X, Y, and U planes. They provide excellent time resolution, in the order of 300 ps.

- **VETOs**

  The VETO system allows to remove tracks outside the main beam spot, the so-called beam halo. It is placed upstream of the target. The system is composed of hodoscopes with a pipe that passes through its center, which lets the main beam spot pass without interacting. The Veto signals are often included to the physics trigger in anti-coincidence, to guarantee a selection of beam particles that are interacting in the target only.

2.4 Target

The target is composed of a cylindrical cell 140 cm long and a radius of 3.5 cm. The cell is filled with pressurized liquid ^{4}He. The target platform is the same as that used in the COMPASS 2022 setup. The target can be polarized by the Nuclear Dynamic Polarization technique using a dipole and solenoid magnets that surround it with a dilution refrigerator and microwave radiation. In 2023, AMBER used an adapted cell filled with liquid helium. Figure 2.3 shows a sketch for the COMPASS 2022 target; the only differences of AMBER 2023 is that the cell is filled with liquid helium and the two central copper disk microwave stoppers are removed.

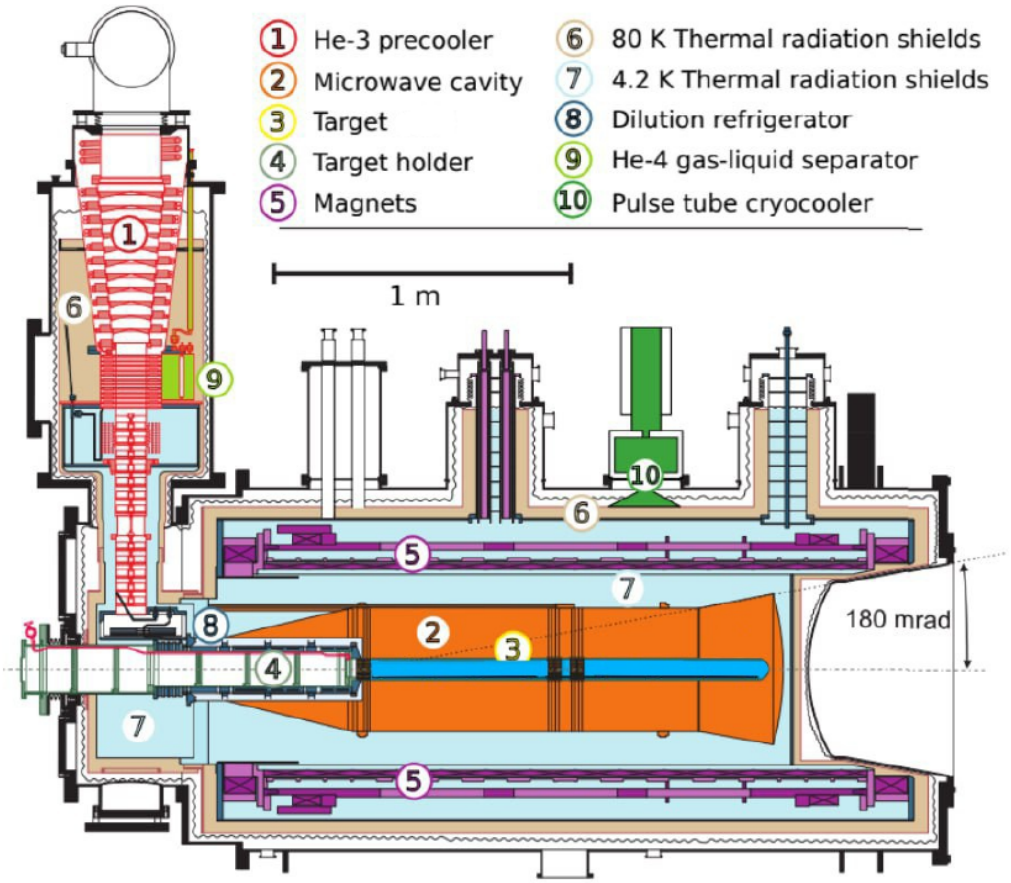

Figure 2.3: Target schematics, including the COMPASS target solenoid/dipole and the dilution refrigerator systems, that in 2023 were not used, remaining as passive. The dilution refrigerator was not used during this data taking.

2.5 Trigger

The beam intensity was tuned to 5×10^5 particles per spill, which is considered low intensity, making it easy to cope with the data acquisition system (DAQ) without pre-scaling of the physics trigger. A random trigger is also present, produced by the beta decay of a ^{22}Na source, used to determine the beam flux. The physics trigger accepts the events where signals in the Beam Telescope compatible with a beam track are in coincidence with no-signals in the beam killer and in the VETO systems, which translates in logical notation to $BT + \overline{BK} + \overline{VETO}$.

- **Beam Trigger**

  Out of the three SciFi stations placed upstream of the target, two of them are used in beam trigger when both send a simultaneous beam signal. A minimum number of hits is required in both of them to fire the beam trigger.

- **Beam Killer**

  The beam killer (BK) is placed 32 m downstream with respect to the target. This detector is used to remove the non-interacting beam. The BK has a circular transverse section with a 3.5 cm radius, the same radius as the target cell.

- **VETO**

The VETO removes beams that are outside the main beam spot, and may not interact in the target, the so-called beam halo. It is placed upstream of the target. The VETO is composed of hodoscopes.

2.6 Spectrometer

The spectrometer is placed downstream of the target and is composed of two smaller spectrometers: the large angle spectrometer (LAS) and the small angle spectrometer (SAS), each one consisting of trackers before and after a dipole magnet (SM1 and SM2, respectively). The momentum of the charged particles is measured from the bending angle in the known vertical magnetic field. There are three types of detectors: Very Small Area Trackers (VSAT), Small Area Trackers (SAT), and Large Area Trackers (LAT). Figure 2.4 shows the COMPASS 2022 schematics; the figure is not in scale. Besides the trackers, the spectrometer also includes a set of electromagnetic and hadronic calorimeters in each of its two stages. Both the calorimeters and the RICH are used for particle identification.

2. EXPERIMENTAL SETUP

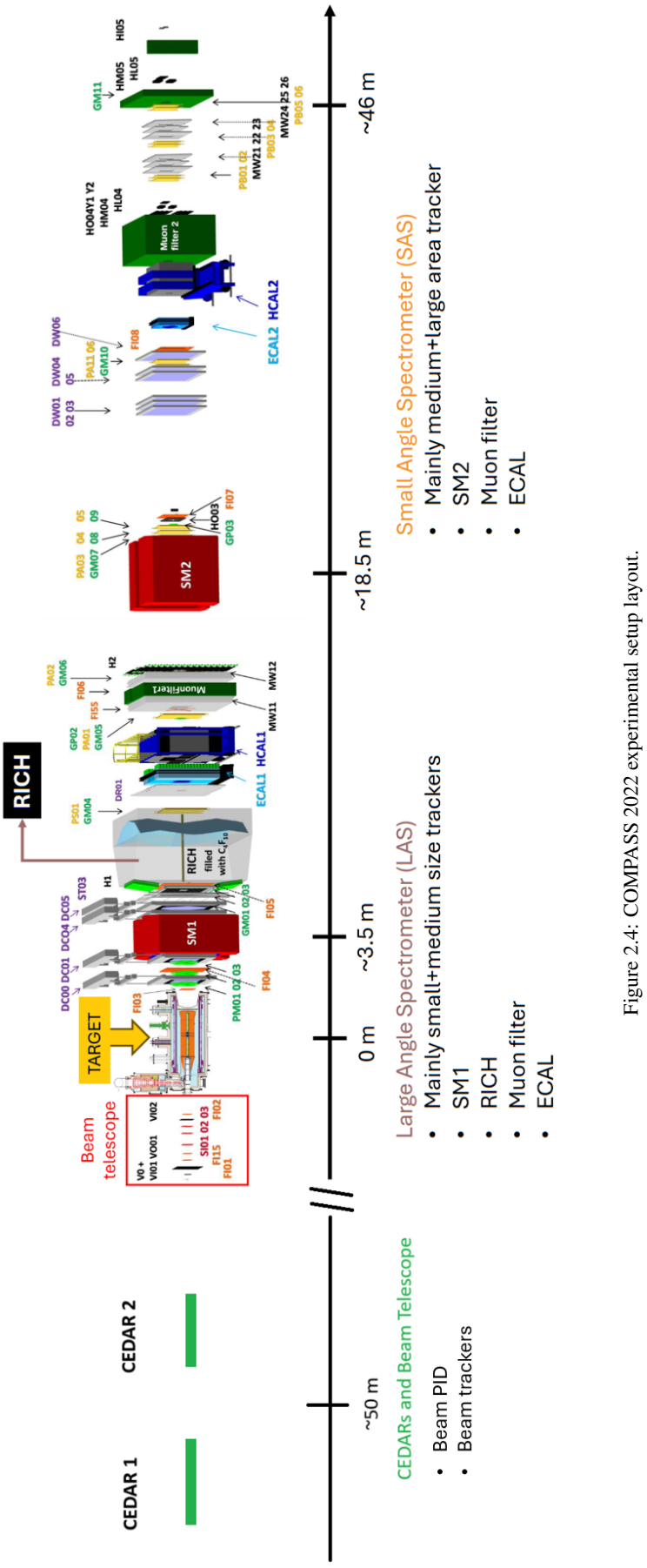

Figure 2.4: COMPASS 2022 experimental setup layout.

2.6.1 RICH

The Ring Imaging CHerenkov (RICH) is placed downstream from the SM1 and includes a large radiator volume of C_4F_{10} gas. It is a detector used in particle identification through Cherenkov radiation. The minimum momentum threshold for particle identification depends on the particle mass: 2.5 GeV/c for pions, 9 GeV/c for kaons, and 17 GeV/c for protons/antiprotons [9]. The detector has a length of 3 m, a width of 6 m, and a height of 5 m. It uses a mirror system to focus the Cherenkov photons on the photon detectors, that are of various types: Multiwire proportional chambers (MWPC) with CsI photo-cathodes, multianode photo-multipliers (MAPMTs) and Thick GEMs.

Good RICH efficiencies are required to obtain reliable particle identification and depend on the momentum and the polar angle of the identified particle. The efficiency values were previously calculated by D. Giordano in [8]. Figure 2.5 shows the schematics for the RICH detector.

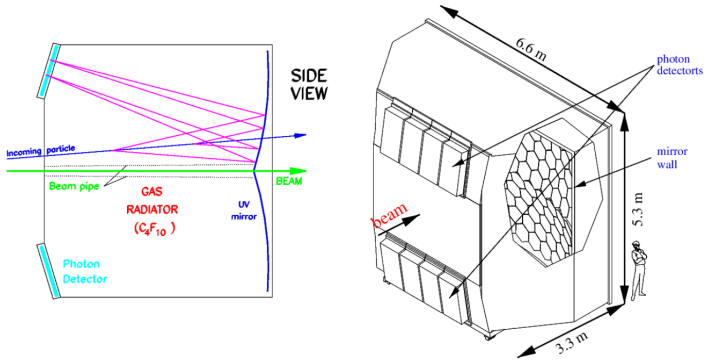

Figure 2.5: Schematics of RICH detector.

2.6.2 Scintillating Fibers in the Spectrometer

The scintillating fibers or SciFi are VSAT with high granularity (16 cm^2-144 cm^2) and high time precision (350 ps-450 ps). There are 7 stations across the spectrometer with 4 scintillating-fiber planes each.

2.6.3 Micro-Mesh Gaseous Structure

The micro-mesh gaseous structure (MP) is a small area tracker placed in front of the SM1 in the LAS. Each station is composed of four detectors with different orientations: horizontal, vertical, and two rotated by ±45deg with respect to the vertical plane. The MP's have an area of 40x40 cm with a central zone of 5 cm in diameter where a pixel structure provides even better space resolution. It has a spatial resolution of 90 μm and a time resolution of 9 ns.

2.6.4 Drift Chambers

The Drift Chambers (DC) are large area trackers composed of 8 wafers, with 4 planes, rotated by 0, 90 or ±20 deg between each other. The average spatial resolution of a single DC layer is 270 μm, and the efficiency is above 95%. It has a central dead zone of 30 cm. Figure 2.6 shows the schematics of the DCs.

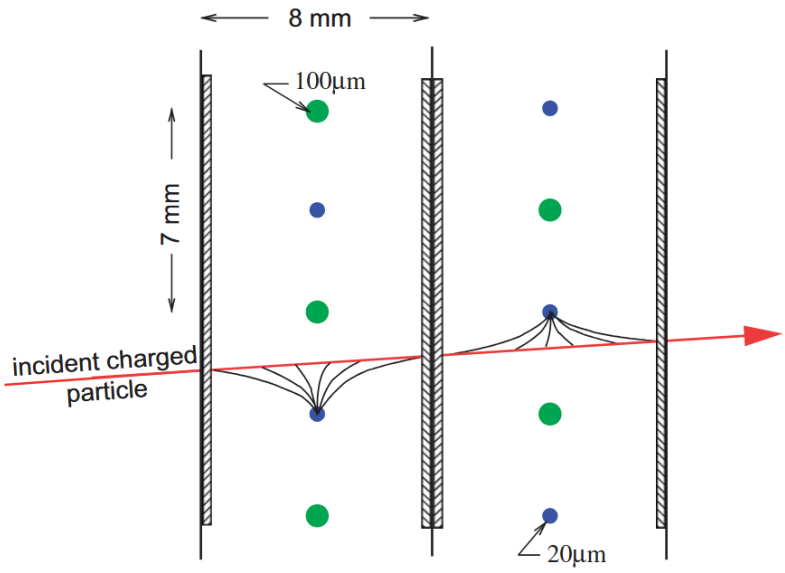

Figure 2.6: Schematics of a Drift Chamber detector. Taken from [7].

2.6.5 DAQ

The data is recorded by the Data AQuisition system (DAQ). Besides the supervision of all the detectors readout, the inner layers of the system consist of a large number of readout buffers (ROBs) that collect the signals from each of the detectors, and four event builders, that concentrate and group the information received per event. The data is stored in the form of "raw data", for offline treatment (by the reconstruction program CORAL).

2.6.6 DCS

Finally, one should also refer the Detectors Control System (DCS), which monitors and commands all the detector's sub-systems, like low voltages, high voltages, gas fluxes, and environment parameters like temperatures, pressure and humidity levels. The DCS of AMBER is a responsability of the portuguese group from LIP. The detector control system fullfils two main functions: monitoring and control of the equipments. The system is quite complex, extending from the hardware interface to devices like power supplies, programmable logic controllers, sensors, etc, to the closest proximity with the researchers on shift, via the graphical user interface (GUI). This so-called "supervision layer" was first build for the COMPASS experiment, and recently adapted to AMBER, using an industrial controls dedicated software, WinCC-OA (previously called PVSS). The DCS is also denominated slow control, since read/write and controls submission happen at a human time scale in the order of the second, in contrast to the high energy physics processes under study, that occur at the nanosecond or lower scale. Parameters like high-voltages, low-voltages, fluxes, pressures, temperatures, magnetic fields, on/off states, and many more, are constantly monitored, with their time trends being recorded "on change", an alarms system guaranteeing any significant variations are visible and audible to the experts. Automatic operations of recovery or transition to safe mode are also programmed. The DCS is transversal to the whole experiment, and it is crucial to guarantee the stability and quality of the data taking. Figure 2.7 shows the Graphical User Interface of the DCS.

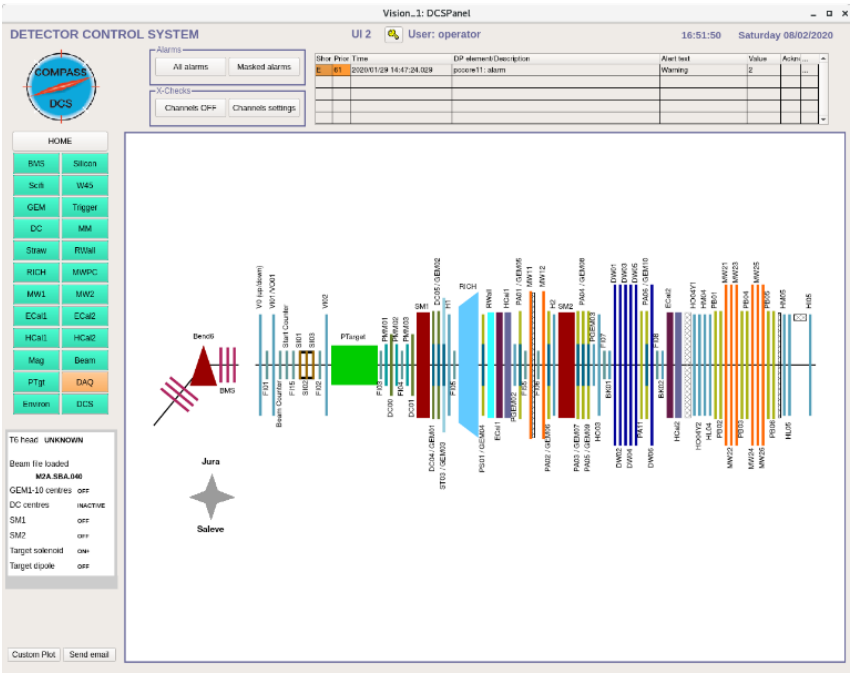

Figure 2.7: Graphical User Interface of the DCS.

Chapter 3

Data Analysis

After the collection of raw data during the period from 19/05/2023 to 24/05/2023, which corresponds to W01, detector experts performed the energy and time calibration and the offline alignment of the detectors with respect to one another. Track and vertex reconstruction from detector signals were performed in the CORAL software; data were stored in mini Data Summary Trees (mDST) root files.

Figure 3.1 shows the analysis flow.

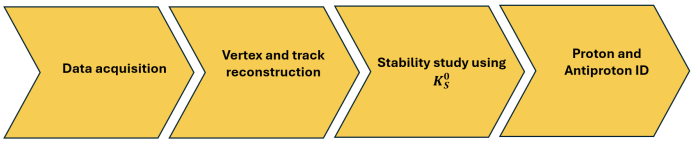

Figure 3.1: Analysis Workflow

PHysiscs Analysis Software Tool (PHAST) is the framework for data analysis on the level of mDST used in COMPASS and AMBER experiments. After running PHAST over the mDST root files, useful information was stored in two ROOT trees: one for event data and the other for track data. After this step, quality cuts were applied in order to ensure a balance between good reconstruction and maximum sample size. All of the plots shown in this section had all of the other cuts applied, except for the one under study.

3.1 Event selection

1. Bad runs and spills rejection
   Stability studies were performed beforehand by D. Giordano [8] on the same reconstructed data sample. After that, a list of bad spills and runs was produced and directly applied in PHAST, such that the corresponding events were skipped.

2. Best Primary Vertex selected
   Only vertices tagged by CORAL as the best primary vertex were included. This cut was applied at the PHAST level. A primary vertex includes a beam track. The best is the one among all primaries that has the lowest spatial reduced χ^2.

3. Physics Trigger
   Trigger information was kept in a bitmap called the trigger mask. The physics trigger was composed of the beam trigger and the anti-coincidence with the beam killers and the VETO signals (see section 2.5). A random trigger was also present; the selection of events was inclusive, meaning that events with a physics trigger bit and a random trigger bit passed this cut.

4. Time in Spill (TiS) in [1.2,5.4] s
   A spill is a period of approximately 5 seconds with constant beam intensity. TiS was the time at which the event occurred in relation to the start of the spill. The limits were placed to remove any border effects.

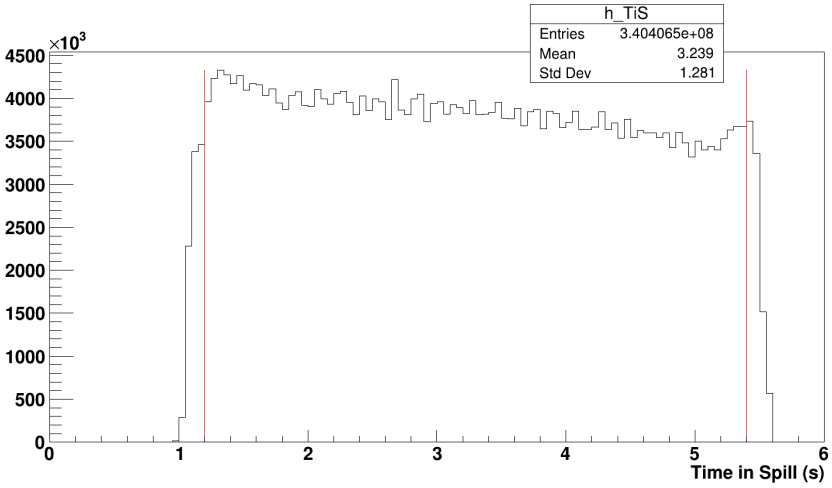

Figure 3.2: Distribution of time in spill for events. The red lines show the upper and lower limits of the cut.

5. Z vertex position inside the target
   As it will be mentioned in Chapter 4, the resolution for the Z vertex position was calculated by using the Monte Carlo simulation and the formula $\Delta Z = Z_{reconstructed} - Z_{generated}$. The ΔZ distribution was plotted in 3.3a and fitted with a sum of a Gaussian function and a second-order polynomial function; its standard deviation gives us the resolution. Figure 3.3a shows that the beam is approximately Gaussian shaped and well centered with the target (p1 of the fit), the standard deviation of this distribution is $\sigma \approx 0.4$ cm (p2), so we considered a cut of 5σ. Figure 3.3b shows a smearing effect around 2 cm and a mismatch between the MC reconstructed vertices and the real data, which indicates that the simulation does not yet describe real data completely. A Z-bias effect is clearly observed in the shift between the real data and the reconstructed MC data in the target cell's window, around the 80 cm position.
   To ensure that the selection includes a flat distribution of both RD and MC, a cut was made 5σ from the edges. Since the target's position is $[-70, 70]$ cm, the final cut was $Z \in [-68, 68]$ cm.

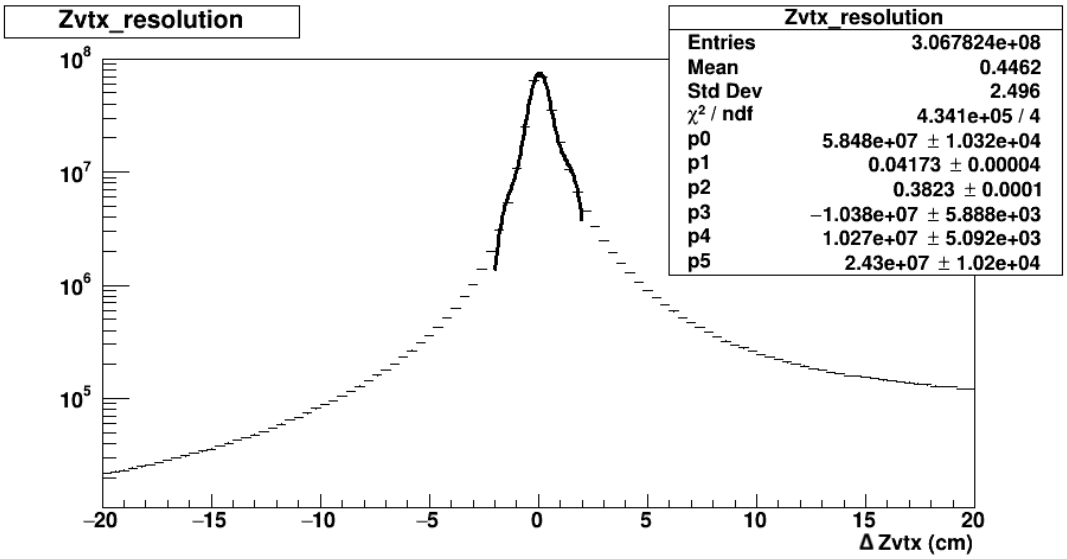

(a) ΔZ

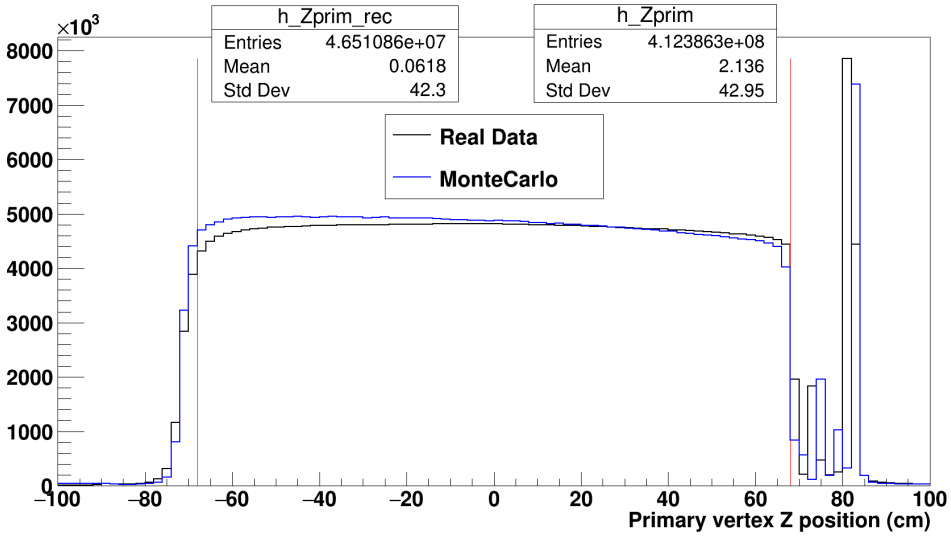

(b) Z

Figure 3.3: (a): Distribution of ΔZ in cm fitted with a sum of a Gaussian function and a second-order polynomial function; (b): Distribution of Z vertex for both Real Data and Monte Carlo simulations.

6. X and Y vertex position inside the target
   Figure 3.4 shows the distribution of X and Y positions for primary vertices for bothRDand MC. It also shows a fit for the RD, in which we can observe $\sigma \approx 0.4$ cm (p2) for both X and Y. The beam spot only illuminates a radius of approximately 1.2 cm. So by applying a cut of 3σ on the radius ($r = \sqrt{X^2 + Y^2}$), we can ensure that we selected the spot on the target where the beam is passing. Additionally, this cut guarantees that only the target material effectively illuminated by the beam is taken into consideration when cross sections are computed.

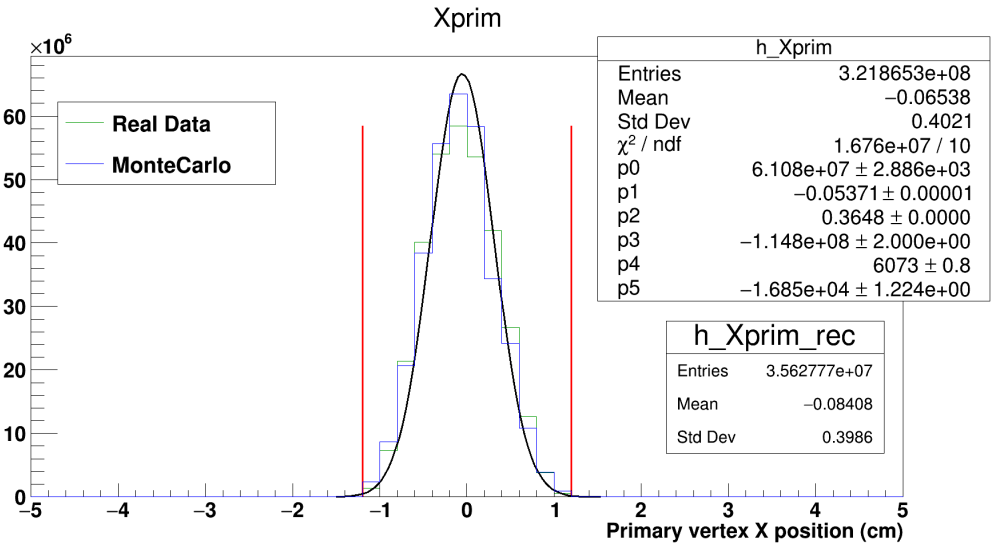

(a) X

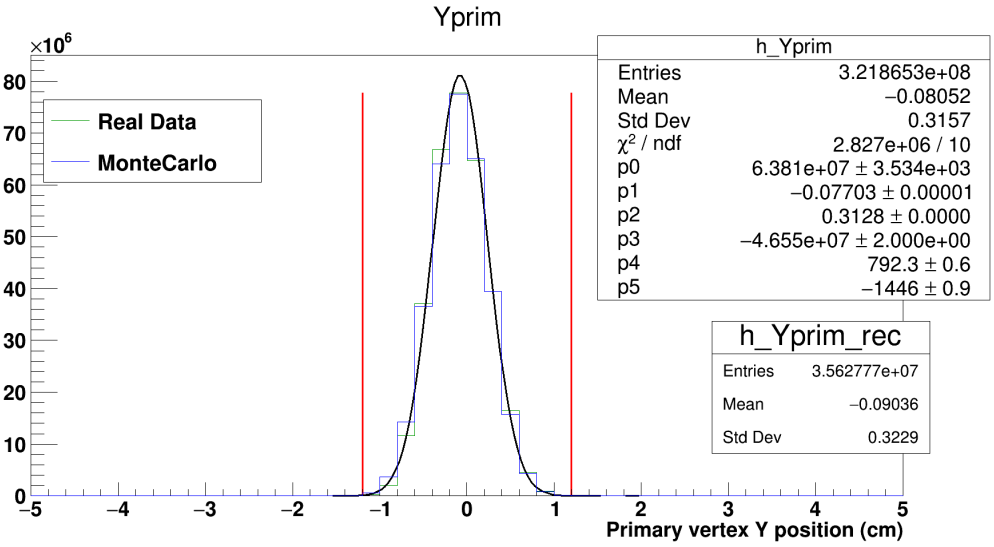

(b) Y

Figure 3.4: Distributions of X (top) and Y (bottom) positions for primary vertices

7. Beam quality

   Beam quality was evaluated with a requirement on the minimum number of hits associated to tracks, in Silicon and SciFi detectors placed in the beam telescope. For the Silicon detectors, a minimum of 9/12 hits was required to consider the beam track good.

   In the beam telescope, there were 3 SciFi detectors; each beam track needed to have at least 5/7 hits in these detectors to be selected. This was illustrated in Figure 3.5.

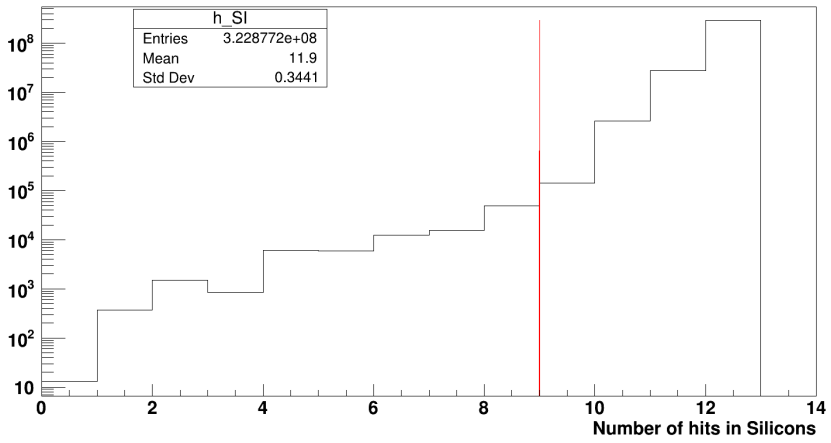

(a) SI

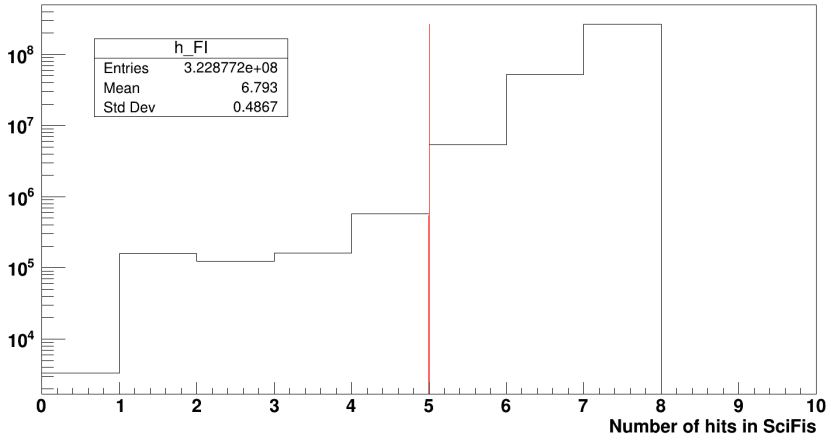

(b) FI

Figure 3.5: Distribution of number of hits in Silicon detectors (top) and in Scintillating fiber detectors (bottom).

8. Beam track passes through the whole target length.
   Each beam track was extrapolated along the Z-axis to the entry and the exit of the target. We required that X and Y positions at the target entry and exit have to be within the radius cut established in item 6.

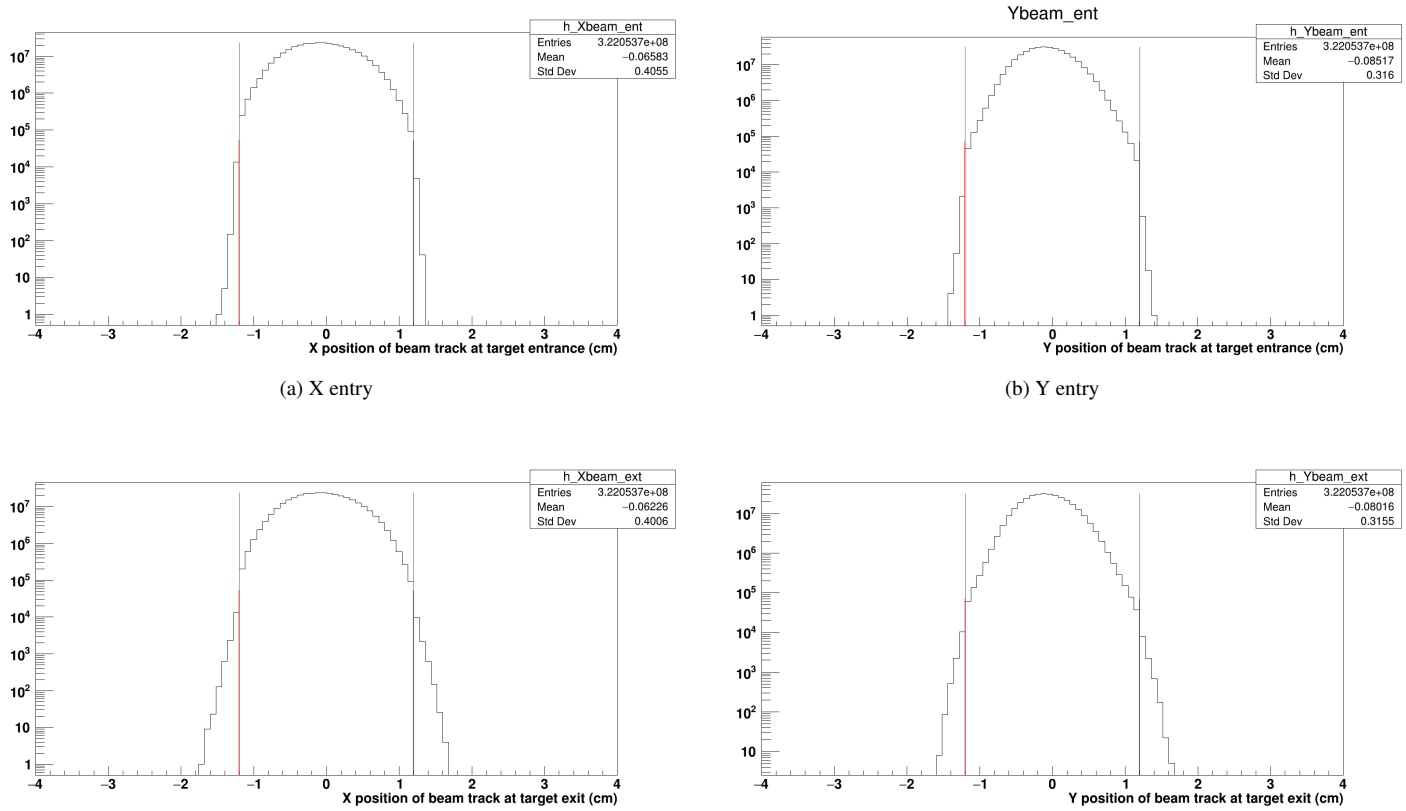

(a) X entry

(b) Y entry

(c) X exit

(d) Y exit

Figure 3.6: Distributions of the beam track X and Y positions at target entry and exit.

9. Proton beam identified

   Both CEDARs have a diaphragm aperture that is adjusted to only let the proton Cherenkov ring pass. Each CEDAR has 8 PMTs. By requiring at least 6 PMTs (6/8) to fire, we identified $\left(\frac{\#NHits\geq 6}{\text{all entries}}\right)_{CEDAR1} = 74.04\%$ and $\left(\frac{\#NHits\geq 6}{\text{all entries}}\right)_{CEDAR2} = 77.33\%$, which is considered a good proton identification ratio since, at 190 GeV/c, the positive hadron beam should be a mixture of 74.6% protons, 24% π^+ and 1.4% K^+ [9].

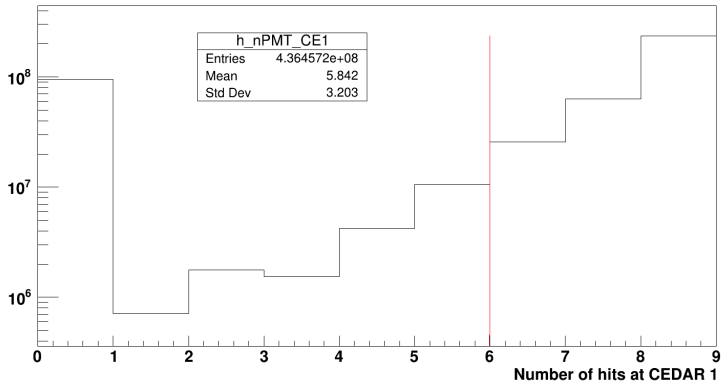

(a) CEDAR 1

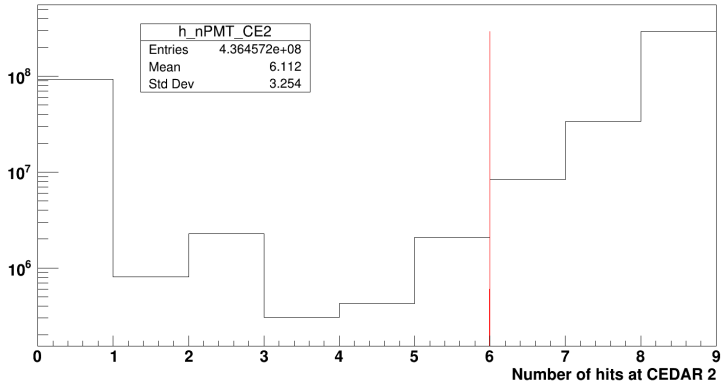

(b) CEDAR 2

Figure 3.7: Distribution of number of hits in the CEDAR's PMTs.

10. Number of outgoing particles ≥ 2
    The number of outgoing particles from the best primary vertex must be higher than 1 to ensure that elastic events are excluded.

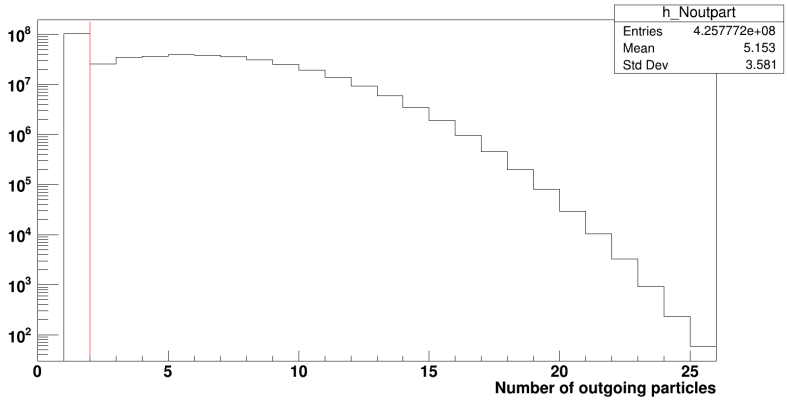

Figure 3.8: Distribution of the number of outgoing particles from each vertex.

The cut flow with its respective fraction and sample size is shown in Table 3.1. The number of events corresponds to the entire statistics in period W01.

Table 3.1: Event selection criteria

Cut name	Number of events	Fraction (%)
All events	1018227136	100
Physics trigger	1018173952	99.9
TiS window	962480832	94.5
Z vertex position	598473280	58.8
X and Y vertex position	578186368	56.8
Beam quality	575996224	56.6
Beam track in target	575049920	56.5
Proton beam identified	425777216	41.8
Number of outgoing particles	321808640	31.6

3.2 Tracks selection

From the selected vertices, we looped through all of the outgoing particles and applied cuts to ensure proper hadron reconstruction. Proton identification was performed at later steps.

1. χ^2/ndf< 10
   This is a standard quality cut to select only well-reconstructed outgoing tracks. Figure 3.9 shows the distribution for χ^2/ndf, only tracks below the red line pass the selection.

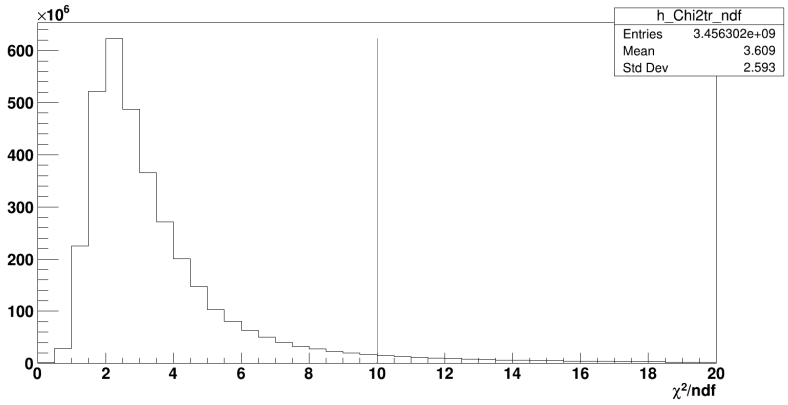

Figure 3.9: χ^2/ndf of the tracks selected. This reduced χ^2 is computed from the distance to track of the detector hits that were associated to the given track.

2. Z_{first} and Z_{last}
   The first measured point for the outgoing tracks should have Z position before the first spectrometer dipole (SM1), which is located at 350 cm. The last measured point should be after SM1. Figure 3.10 shows that this second cut was redundant. These cuts served to ensure good momentum reconstruction.

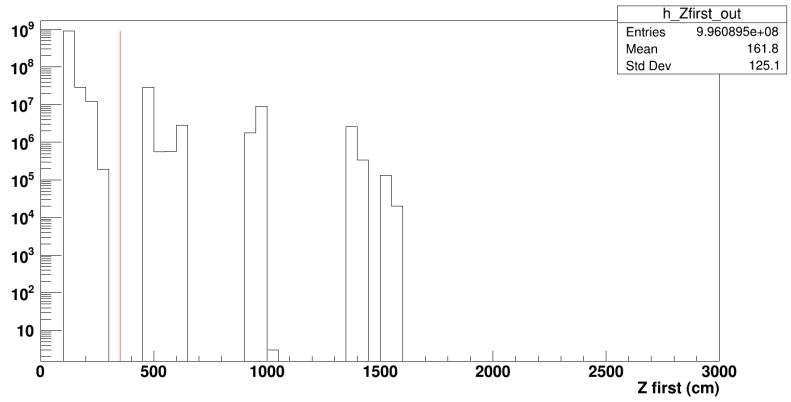

(a) Z_{first}

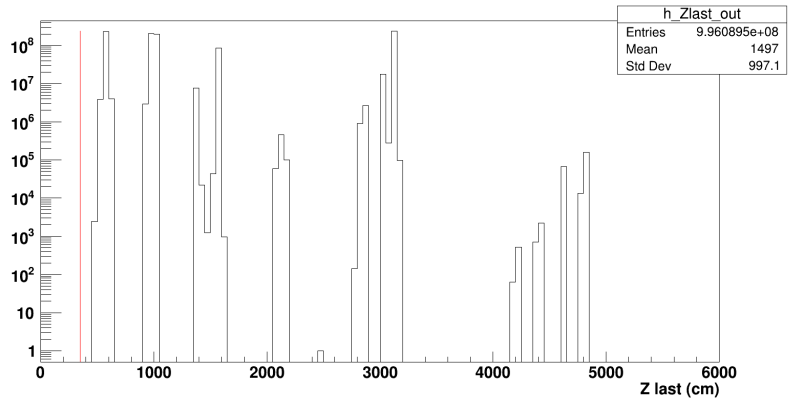

(b) Z_{last}

Figure 3.10: Distributions of Z_{first} (top) and Z_{last} (bottom). The red line is placed at $Z = 350$ cm.

3. Radiation length

   The number of radiation lengths crossed by the tracks along the spectrometer (between Z_{first} and Z_{last}) was required to be less than 10 to ensure that muons were excluded, since we are interested in hadron production. Figure 3.11 shows the distribution for X/X_0 and the selection limit in red.

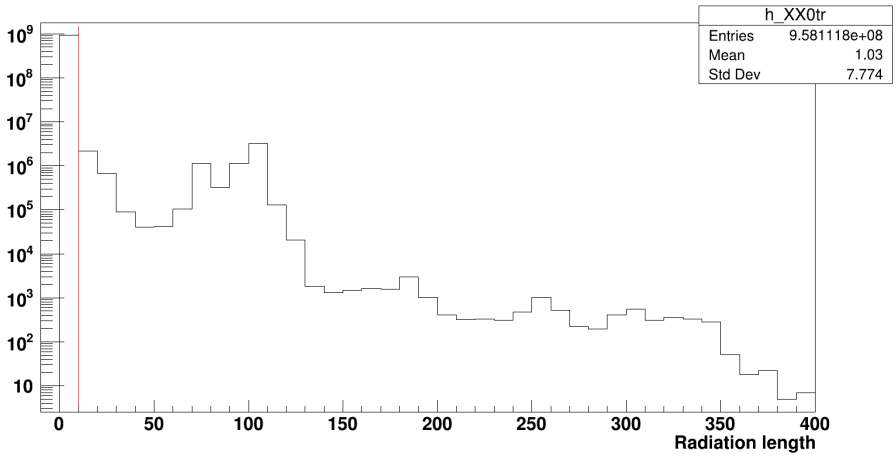

Figure 3.11: Distribution of the tracks' X/X_0 in the spectrometer.

4. Timing

The track had a measured mean time. The mean time of the track is a weighted average of hits' time, using the time resolution of the detectors as weights. Only tracks that crossed detectors precise enough in time have this quantity defined.

Figure 3.12 shows the distribution of the mean time for outgoing tracks; the value in overflow shows the number of tracks without a defined mean time (initialization values), which remains small but non-negligible. This figure also shows that the distribution has two bumps; the one on the left belongs to tracks that begin in the MP01 detector, clearly off-time. These results indicate that this detector needs to be time-calibrated.

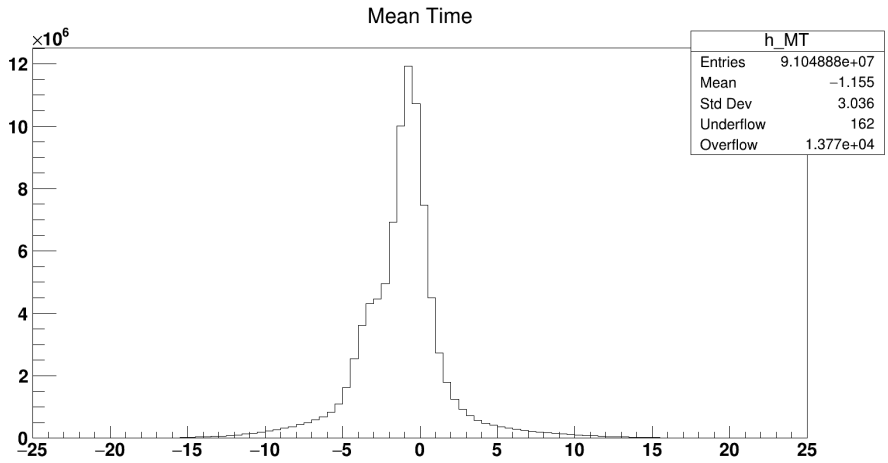

Figure 3.12: Distribution of the timing of the outgoing tracks.

In Figure 3.13 the tracks timing was studied in more detail. The tracks were divided in two samples, those that start in the scintillator fiber detector FI03 ($Z_{First} < 137$ cm) are correctly synchronized with the trigger time ($t = 0$ ns), and are typically tracks emitted at small angles, given the small dimension of this detector. The tracks in the complementary sample ($Z_{First} > 137$ cm) have their first measured point more downstream, typically at Pixel MicroMega detector MP01, which is not correctly time-calibrated. These latter are tracks that tend to be emitted at larger angles.

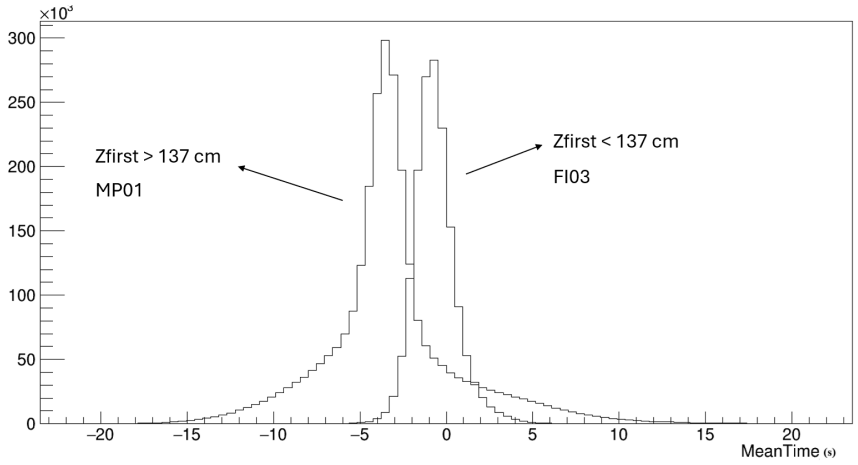

Figure 3.13: Distributions of the timing of the outgoing tracks according to their respective Z_{first}.

5. Track can be extrapolated to the RICH entrance
   The RICH detector, located after SM1, had limited dimensions, and we wanted to accept only tracks compatible with these dimensions. For this data taking, no beam pipe was used at the center of the RICH, a limitation that had been present in COMPASS 2022.

6. Track has RICH data
   Particle identification data in the RICH detector were previously treated and stored with the PHAST PaPid class. RICH information array size should not be 0.

7. Momentum at RICH entrance
   For each particle, the minimum threshold for emitting Cherenkov photons is 2.5 GeV/c for π, 9 GeV/c for K, and 17 GeV/c for p and $\bar{p}$ [9]. Figure 3.14 shows the different identified particles and their respective bi-dimensional distribution of the Cherenkov angle θ_{Ch} measured with respect to the Z axis (rad) versus the crossing particle momentum measured in the entrance of the RICH detector P (GeV/c). The different arches are well defined, which shows that the RICH detector has high efficiency. For the pion population, which has the lowest identification threshold, there is a clear contamination of the electron population in the region $P < 5$ GeV/c, so this value served as the minimum value for this selection. Above the 50 GeV/c value, a smearing effect is visible for hadron identification; this value was used as the maximum threshold.

   After being extrapolated to the RICH entrance, the absolute value of the track's momentum should be in the momentum range $[5, 50]$ GeV/c.

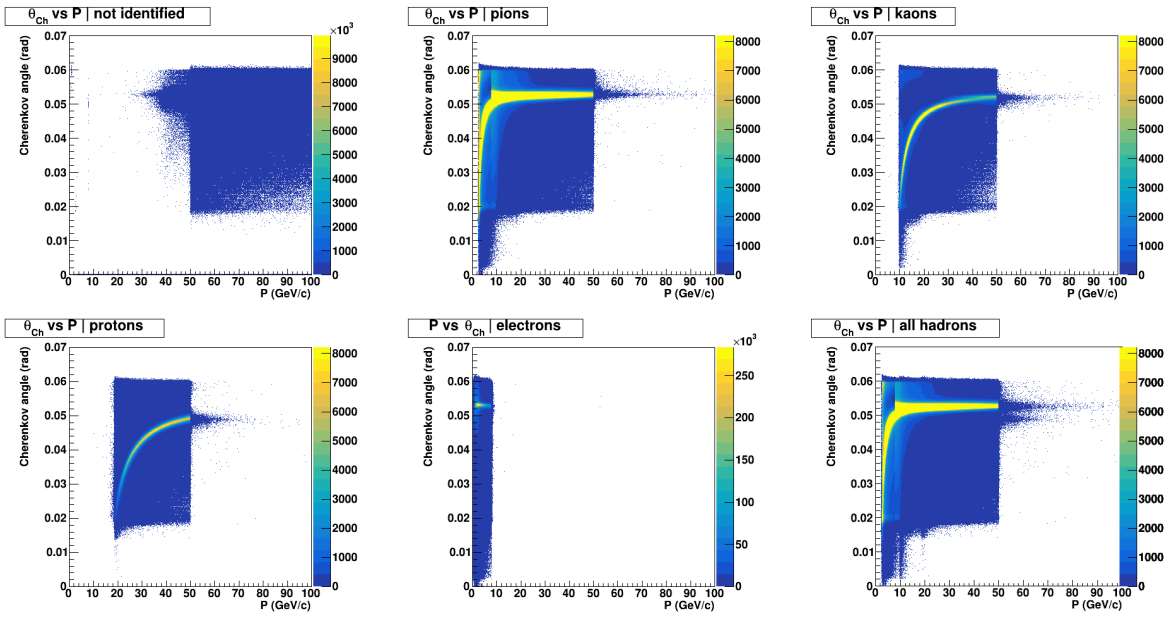

Figure 3.14: Angle of the Cherenkov photons emitted vs Momentum of the crossing particle at RICH entrance. Particle identification was performed using likelihoods from the PHAST PaPid class.

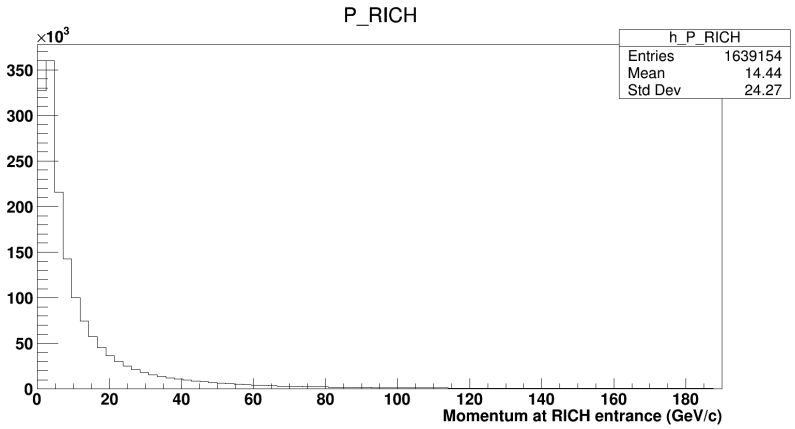

Figure 3.15: Momentum of selected hadron tracks at RICH entrance, before cutting on non-extrapolated to RICH ones.

8. Polar angle at RICH entrance
   $\theta \in [0.01, 0.18]$ rad. Range taken from the RICH matrix. Figure 3.16 shows the distribution of the polar angles at the RICH entrance.

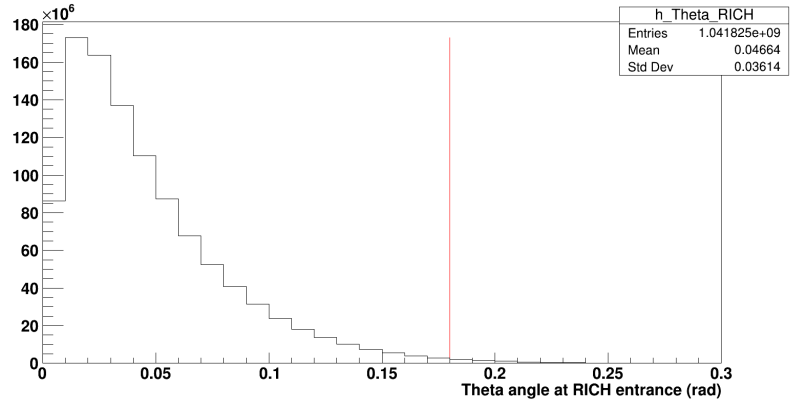

Figure 3.16: Polar angles of the hadron tracks extrapolated to RICH.

Table 3.2 shows each track cut along with the fraction of the sample that remains; these cuts rejected 61 % of the events. The particles' PID will only be used in a later section.

Table 3.2: Tracks selection criteria of the tracks that passed vertex selection.

Cut name	Number of tracks	Fraction (%)
All tracks	2.09×10^9	100
$\chi^2/ndf < 10$	2.00×10^9	95.5
$Z_{first} < Z_{SM1}$ and $Z_{last} > Z_{SM1}$	1.88×10^9	90.1
$X/X_0 < 10$	1.85×10^9	88.3
Defined mean time	1.79×10^9	85.5
Track extrapolated at RICH	1.79×10^9	85.5
Track has RICH data	1.78×10^9	85.2
P at RICH entrance	8.95×10^8	42.8
θ at RICH entrance	8.15×10^8	39.0

Chapter 4

Monte Carlo Analysis

The Monte Carlo simulation was necessary to calculate acceptance corrections, which include geometrical acceptance, reconstruction, detector and trigger efficiencies, as well as to calculate resolutions and decide on histogram binning.

The simulation is performed in 3 steps: first, the physics events were generated using the PYTHIA 8 program [11]; second, the experimental setup was simulated using the TGEANT software, designed to specifically simulate the COMPASS and later AMBER experiments, based on the GEANT4 framework [12]; third, the MC data were saved in ROOT trees similar to the ones used for real data, using PHAST; the generated and reconstructed data were both saved to ROOT trees. DAQ, VETO lifetime, CEDAR, and RICH-1 were not reconstructed, so the PID of reconstructed tracks was taken from MC truth. The beam file was produced beforehand.

4.1 Generated data

The physics process "soft QCD" was generated in PYTHIA 8 by D. Giordano [8], who also prepared the TGEANT simulation, that describes the details of the spectrometer, simulates the passage of generated particles through matter and the interactions occurring in the detectors, while transporting the particles. Several aspects of the real experiment could not be simulated: the MC beam contained only protons, and there was no CEDARs treatment; and the RICH particle identification was as well not simulated.

To apply acceptance corrections to the real data (RD), we needed to ensure that the Monte Carlo correctly reproduces the data, and that the same treatment is applied to the two samples (MC reconstructed and RD), namely that the same geometrical and kinematic cuts are applied.

4.1.1 MC truth event and track selection

MC event selection:

1. Events generated inside the helium target: $Z \in [-68, 68]$ cm
2. Events generated within a 0-centered circle of radius: $r < 1.2$ cm

MC track selection:

1. Outgoing particles with generated momentum $P \in [5.0, 50.0]$ GeV/c

4.2 Reconstructed MC data

The same logic that was applied to the generated events and tracks was applied to the MC reconstructed ones. The same quality cuts that were applied to real data were also applied to the reconstructed MC sample.

4.2.1 Event and track selection

Event selection:

1. Physics trigger: the trigger system was also simulated, and in the selection one requires the physics trigger bit to have fired, regardless of the state of other trigger bits (inclusive selection);
2. MC reconstructed primary vertices must be well inside the helium target region: $Z \in [-68, 68]$ cm
3. and $r < 1.2$ cm
4. The quality of the MC reconstructed beam track is ensured by a significant number of hits associated to the track, along the beam telescope planes: $\#Hits_{FI} \geq 5$ and $\#Hits_{SI} \geq 9$
5. Beam track must cross the target in all its length;
6. # outgoing tracks ≥ 2

Track selection:

1. Outgoing tracks must have χ^2/ndf < 10;
2. $Z_{first} < Z_{SM1}$ and $Z_{last} > Z_{SM1}$;
3. Outgoing particles cannot be muons: $X/X_0 < 10$;
4. Tracks must have a defined mean time;
5. The momentum of the particles must be within the reach of RICH hadron identification: $P \in [5.0, 50.0]$ GeV/c;
6. The polar angle of the outgoing tracks must be compatible with the RICH dimensions: $\theta \in [0.00, 0.18]$ rad

4.3 MC/RD comparisons

This section is dedicated to comparing the Monte Carlo reconstructed sample with the real data and evaluating if the simulation, with the conditions mentioned before, is a good representation of the natural physics processes. All of the histograms plotted in this section passed all of the selection criteria previously mentioned.

4.3.1 Momentum

Figure 4.1 shows the comparison between RD and MC reconstructed as a function of momentum (which means that it is integrated over the other two variables) and their ratio (RD/MC). The data was normalized so it is comparable. We can observe that the simulation is a good representation of the distribution of this variable, with the maximum deviation being approximately 6 % for high momentum negatively charged tracks.

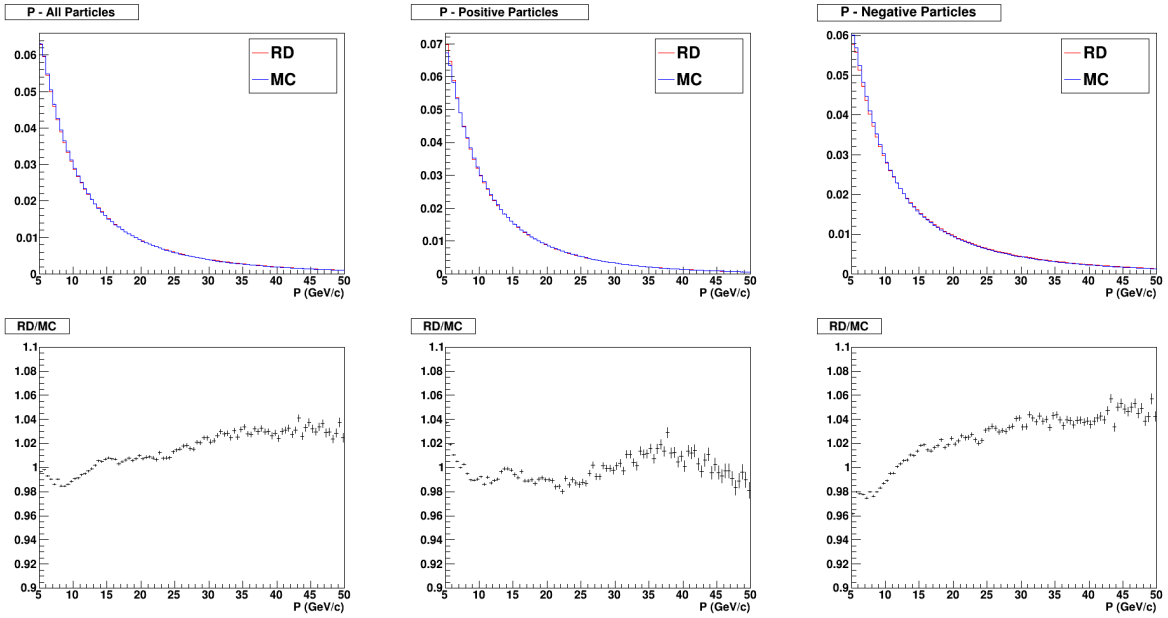

Figure 4.1: Comparison between MC reconstructed data and real data as a function of momentum. The top row shows the comparison of the two, and the bottom row shows their ratio RD/MC.

4.3.2 Transverse momentum

Figure 4.2 plots the comparison between MC and RD data and their respective ratios for the outgoing hadron transverse momentum. The MC simulation does not give a good representation of the real data, with p_T shifted in MC to higher values with respect to the RD, the discrepancy reaching 60% at the lowest and highest p_T values. This discrepancy is likely sensitive to some specific tuning of the intrinsic partons' transverse momentum k_T in the MC.

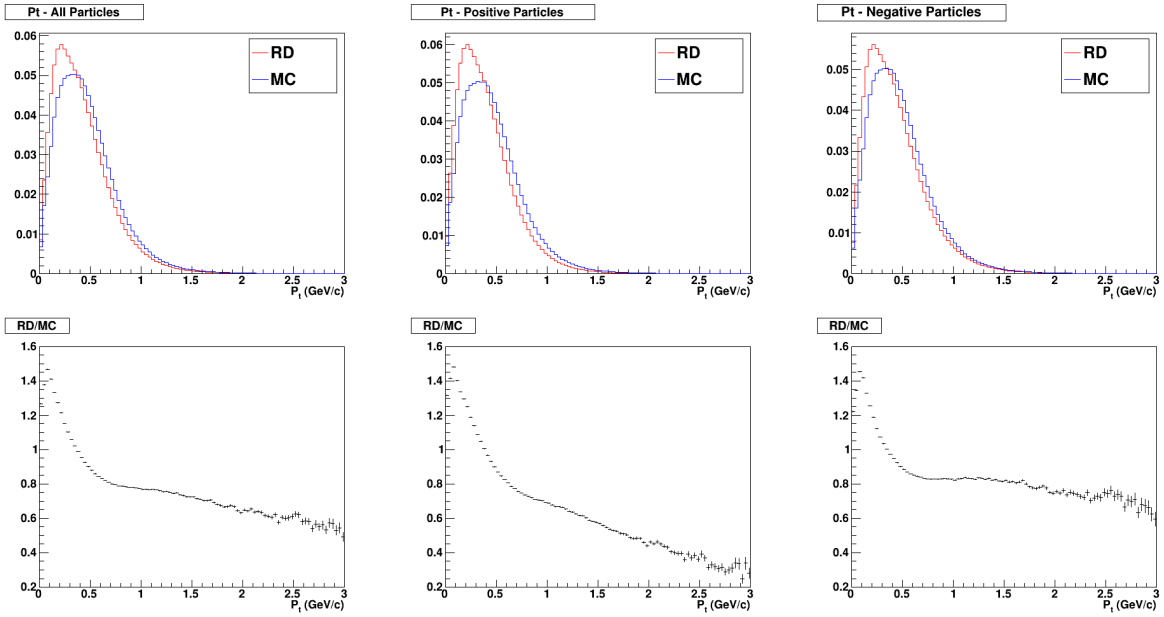

Figure 4.2: Comparison between MC reconstructed data and real data as a function of transverse momentum. The top row shows the comparison, and the bottom row shows the ratio between the two.

4.3.3 X, Y, Z vertex position

The comparison between MC and RD X, Y, and Z positions of the primary vertex is plotted in figure 4.3 along with their respective ratios. For the X and Y positions, if we concentrate only on the central spot that is illuminated by the beam, the maximum difference for the X position is 20% and 10% for the Y position. For the Z position, we can observe a slope in the MC data when compared to RD, with a maximum discrepancy of 20%. As a future work, this MC simulation should be checked to account for the dip in the right-hand side.

Figure 4.3 also shows that the distribution for the X_{vtx} has a "gap" in its distribution; this gap appears when the physics trigger is required during the selection process. Future work is necessary to investigate the reason behind this gap in the distribution.

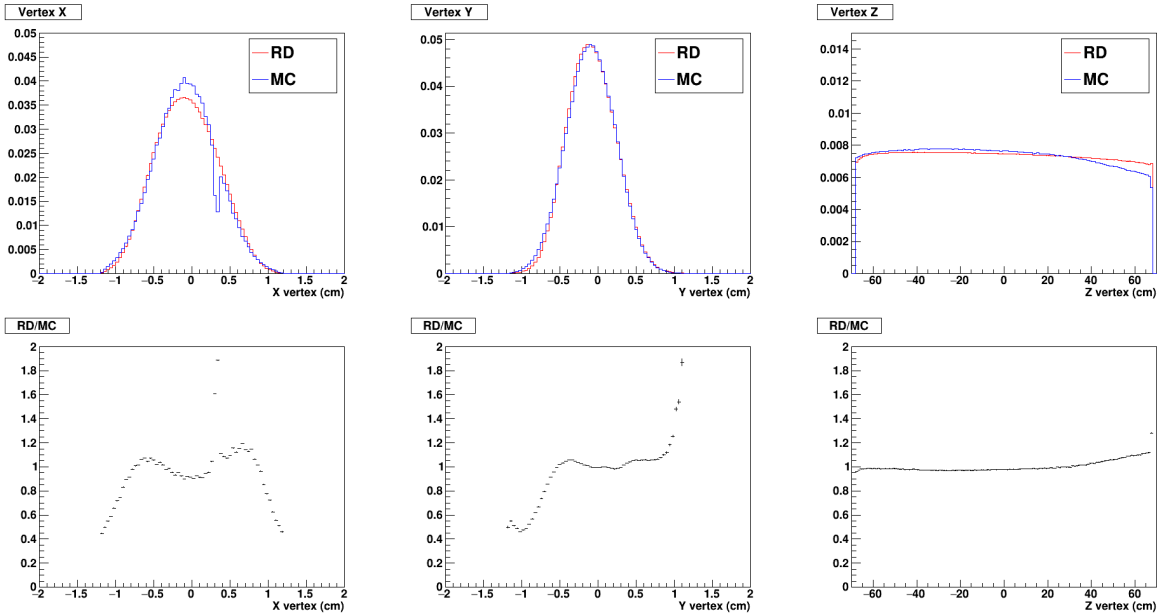

Figure 4.3: Comparison between MC reconstructed data and real data for X, Y, and Z. The top row shows the comparison, and the bottom row shows the ratio between the two.

As we observed, the MC simulation failed to simulate accurately the distribution of transverse momentum and Z vertex position when compared to real data. In order to minimize the impact of possible discrepancies in the final results, we decided to calculate acceptance corrections also in bins of Z vertex position. This discretization approach was done in order for the MC to be a better representation of the real data for each bin of acceptance correction. Note that neither the hadron spectra nor the final cross-section ratios will be plotted in bins of the Z vertex; this procedure was only performed for the acceptance corrections. Although this chapter is dedicated to the Monte Carlo simulation, the binning studies are performed on the real data because the limiting factor is on the side of the RD statistics available for the cross-sections ratio calculation.

4.4 Acceptance Corrections

To calculate the acceptance, *acc*, the hadron spectra are extracted for generated MC events and for reconstructed MC events. The corresponding expression of the acceptance is the following:

$$acc\ (Z_{vtx}, p_T, P) = \frac{\#MCreconstructed}{\#MC\ generated} \tag{4.1}$$

4.4.1 Bin studies

As we have seen in the previous section, there was a discrepancy between the Z vertex position distribution for real data and Monte Carlo reconstructed data. To account for this, acceptance corrections were also calculated in bins of Z_{vtx}.

4.4.1.1 Z_{vtx}

The number of bins should be kept relatively low to ensure maximum sample size, and because the difference between MC and RD is not that lage. It was determined that 3 bins with approximately the

same width are the ideal number. Thus, the bins of Z_{vtx} chosen are [-68,-23,23,68] cm. Figure 4.4 shows the Z_{vtx} distribution along with the bins.

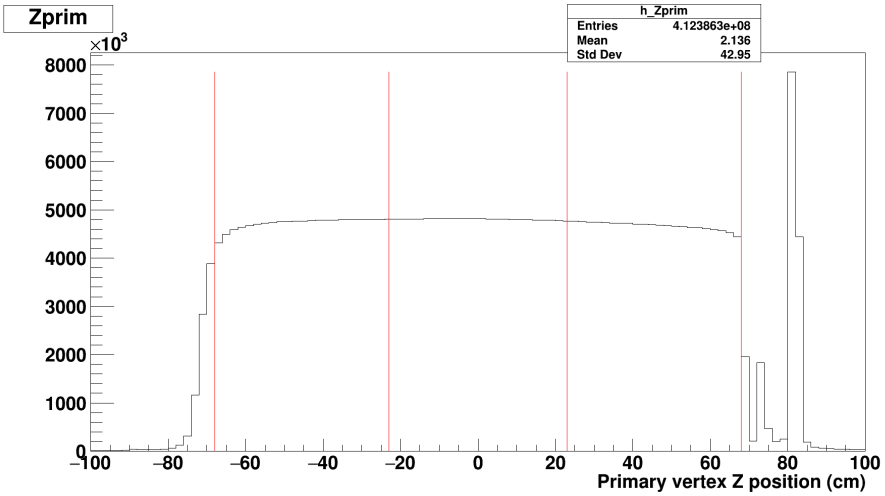

Figure 4.4: Distribution of Z_{vtx}. Red lines indicate the different bins. Real data.

4.4.1.2 Momentum

In the previous chapter, it was determined that the outgoing tracks' momentum at the RICH entrance should be within the range $[5.0, 50.0]$ GeV/c. This range will also be considered for the bins of the momentum at the primary vertex. Figure 4.5 shows the distribution of momentum for the different hadrons. This figure also shows the different thresholds for particle identification at the RICH detector: *approx*5 GeV/c for pions, *approx*10 GeV/c for kaons, and *approx*20 GeV/c for protons. The final values for the cross-section ratios will be plotted as a function of momentum; thus, the bin width should be equal for all bins. We can also observe that pions can be identified below the 10 GeV/c value. Maintaining the same width, new bins will be [5,10,15,20,25,30,35,40,45,50] GeV/c.

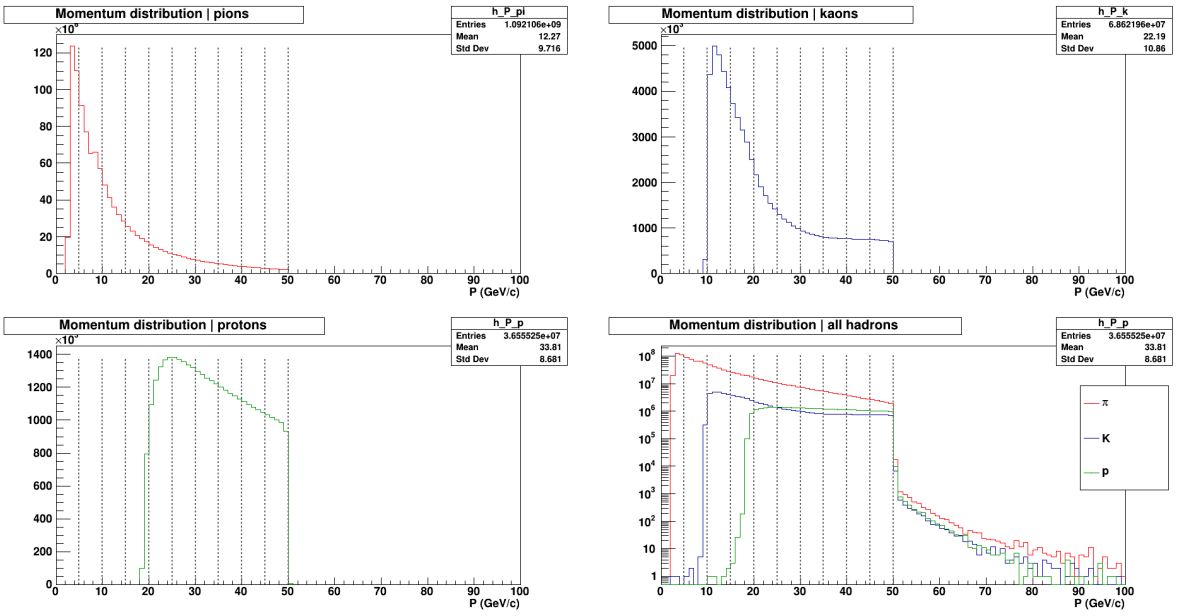

Figure 4.5: Distribution of momentum at the primary vertex for different hadrons. Real data.

4.4.1.3 Transverse Momentum

For the transverse momentum, the bins used by Giordano D. in his thesis [8] were [0.0,0.2,0.4,0.6,0.8,1.0,1.3,1.6,2.0] GeV/c. These bins were also used during these studies; however, figure 4.6 shows that there are enough entries in the 2.0-3.0 GeV/c range to ensure that it is possible to add this bin.

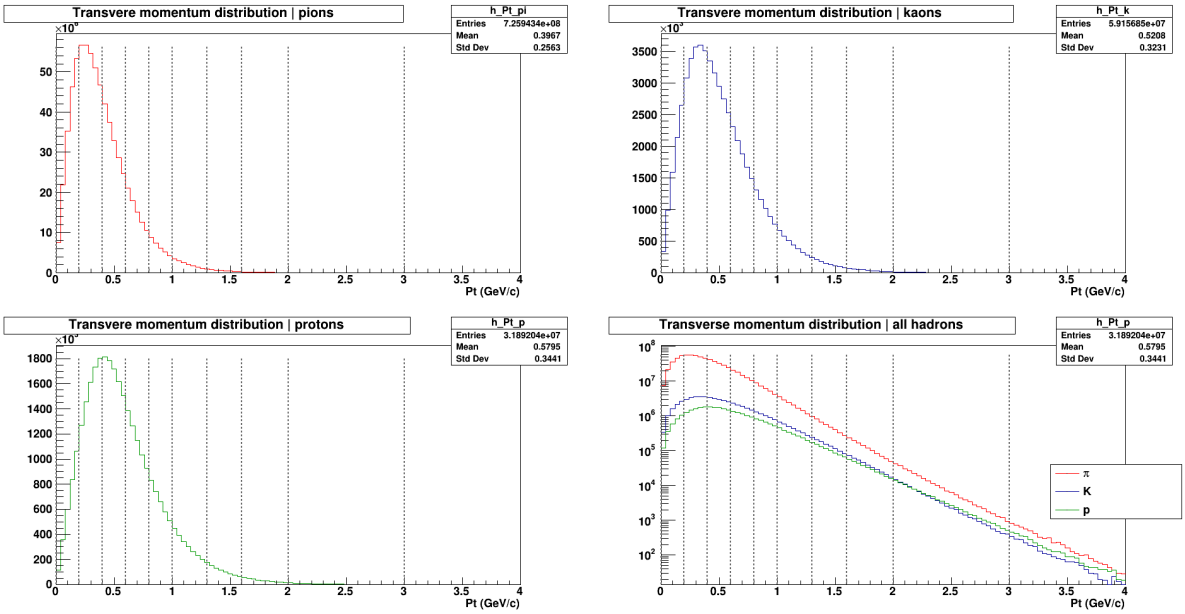

Figure 4.6: Distribution of transverse momentum for different hadrons. Real data.

New bins will be [0.0,0.2,0.4,0.6,0.8,1.0,1.3,1.6,2.0,3.0] GeV/c.

Now we can compute the acceptance in 3 dimensions:

- 3 bins of Z_{vtx} : $[-68, -23, 23, 68]$ cm;
- 9 bins of P : $[5, 10, 15, 20, 25, 30, 35, 40, 45, 50]$ GeV/c;
- 9 bins of P_t: [0.0, 0.2, 0.4, 0.6, 0.8, 1.0, 1.3, 1.6, 2.0, 3.0] GeV/c.

4.4.2 Acceptance Corrections

For each particle, acceptance corrections are calculated in 27 histograms (3 bins of Z_{vtx} $\times$ 9 bins of P_t) as a function of P. In this Monte Carlo there was no simulation of the RICH particle identification. MC truth was used to identify each particle type (that is, one assumes an efficiency of the RICH PID of 100%).

Since the size of the generated Monte Carlo sample is limited, the relative error on acceptance will be used to evaluate if each bin is selected for ratio calculation or discarded.

The criteria for a bin to be selected are:

1. Every bin should have at least 100 entries in the reconstructed and generated histograms.

2. Relative uncertainty should not surpass 15%.

3. Bin must be within the RICH identification range.

After the criteria analysis for each (Z_{vtx}, P, P_t) bins, it will be decided if they are selected or not to be used in the subsequent calculations. In the following plots, a bin that does not meet at least one of the criteria will be etched in gray.

4.4.2.1 Pions

Figure **??** shows the relative error of the acceptance, Δacc, for pions. For all bins of Z_{vtx}, the bin corresponding to $P_t \in [2.0, 3.0]$ GeV/c and $P \in [5, 10]$ GeV/c does not have more than 100 entries, so it will not be used further in analysis. All the other bins that also have less than 100 entries, such as $Z_{vtx} \in [-68, -23]$ cm, $P_t \in [2.0, 3.0]$ GeV/c, $P \in [10, 15]$ GeV/c and $Z_{vtx} \in [-68, -23]$ cm, $P_t \in [1.6, 2.0]$ GeV/c, $P \in [5, 10]$ GeV/c will be selected due to failing the criteria for only one Z_{vtx} bin.

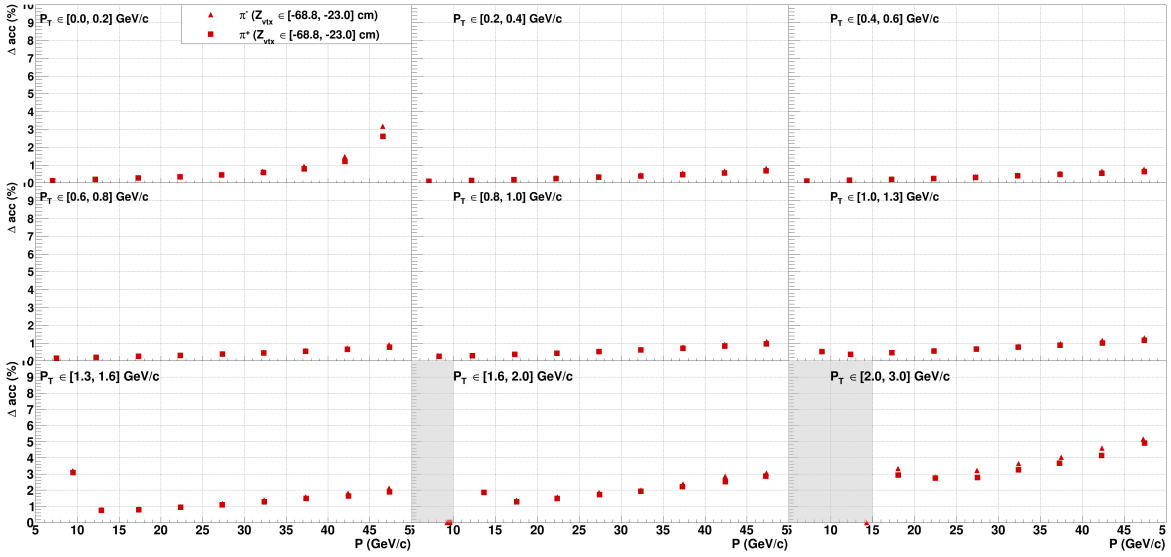

(a) $Z_{vtx} \in [-68, -23]$ cm

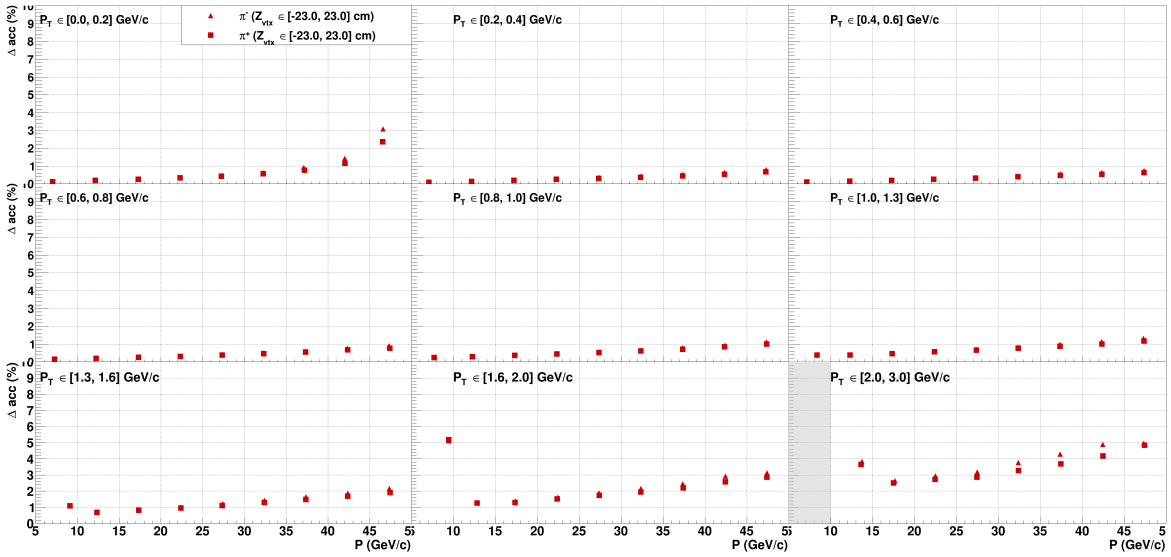

(b) $Z_{vtx} \in [-23, 23]$ cm

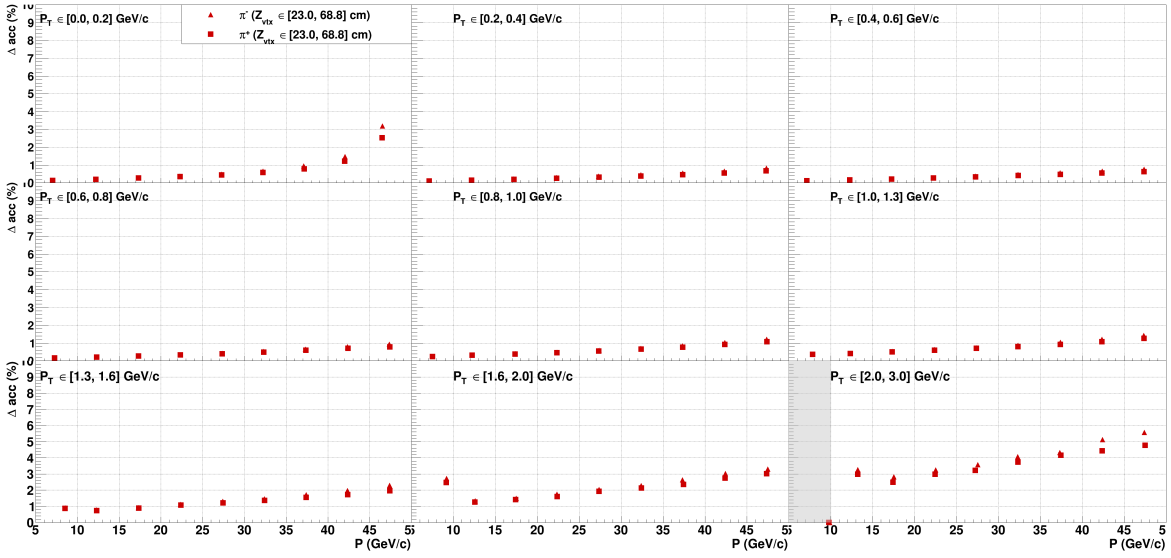

(c) $Z_{vtx} \in [23, 68]$ cm

Figure 4.7: Distributions of the **acceptance relative error** for the different Z_{vtx} bins for **pions** as a function of momentum in bins of transverse momentum. The two different charges are also plotted together.

The 3-dimensional acceptance corrections are plotted in figure 4.8, with error bars displayed, although they are not visible. We can observe that the acceptance is higher for higher transverse momentum and that it drops with P.
We can also observe a systematic difference in the acceptance between tracks that are produced in more upstream regions of the target and tracks produced more downstream. This is likely a geometric effect of the acceptance.

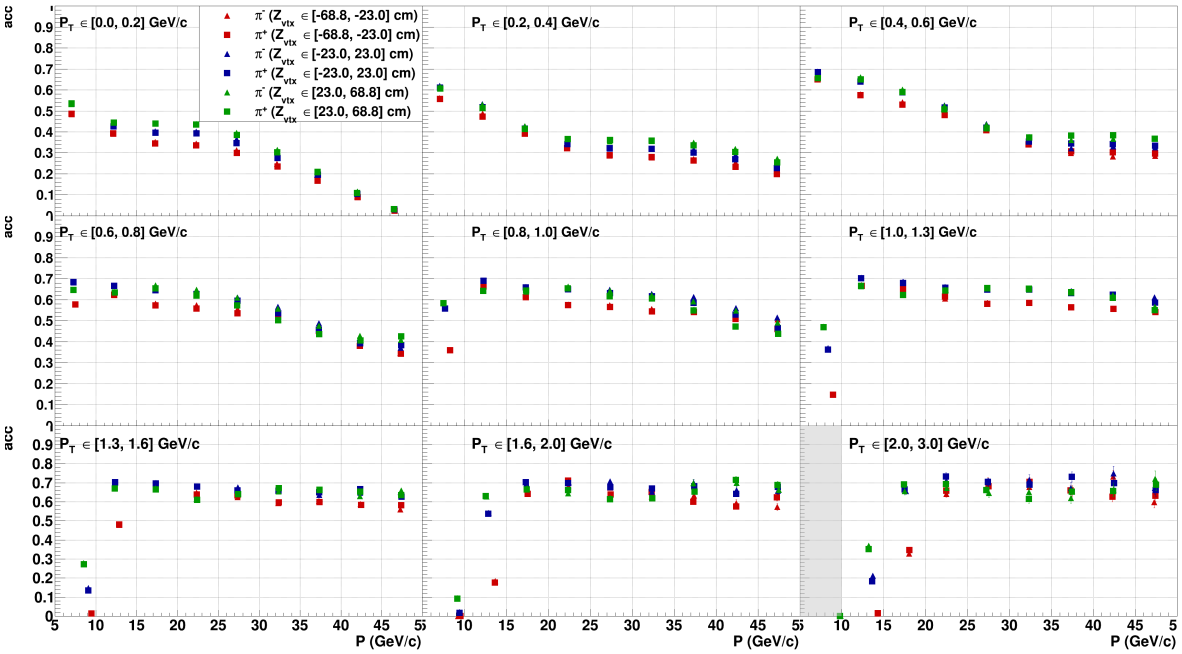

Figure 4.8: **Acceptance** corrections for **pions** as a function of momentum in bins of transverse momentum and Z_{vtx}.

4.4.2.2 Kaons

The relative error for the acceptance for kaons is plotted in 4.9. The RICH detector can only identify kaons above the $P_{min} > 9.3$ GeV/c threshold [3]; consequently, we expect the $[5.0, 10.0]$ GeV/c bin to have fewer entries compared to the others. For all 3 Z_vtx bins, the $P \in [5, 10]$ GeV/c bin for both $P_t \in [1.6, 2.0]$ GeV/c and $P_t \in [2.0, 3.0]$ GeV/c has less than 100 entries and will not be selected. The bin $Z_{vtx} \in [-68, -23]$ cm, $P_t \in [2.0, 3.0]$ GeV/c, $P \in [10, 15]$ GeV/c bin also has fewer than 100 entries and will not be selected.

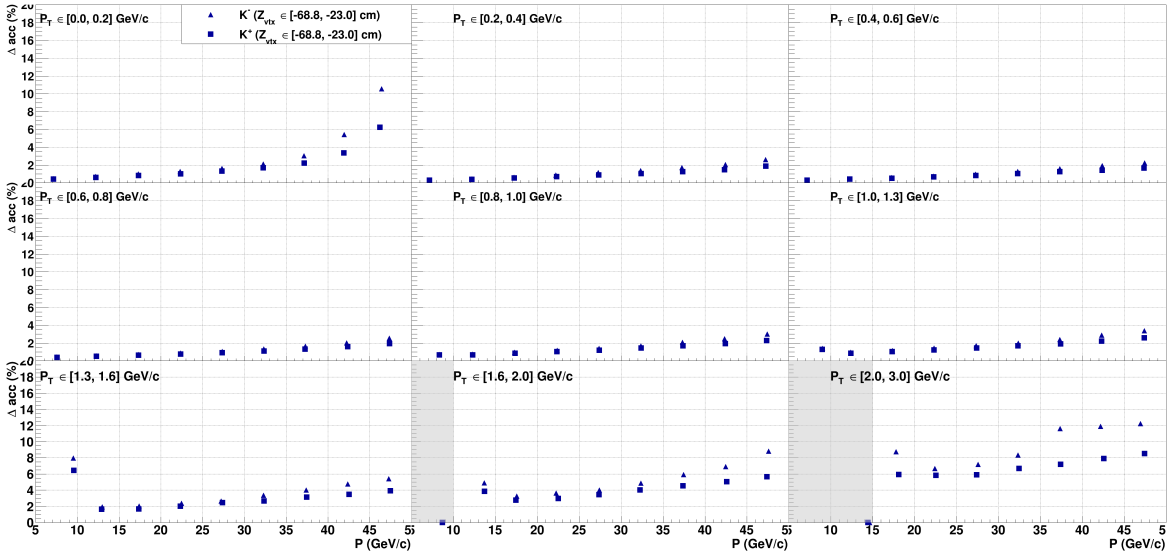

(a) $Z_{vtx} \in [-68, -23]$ cm

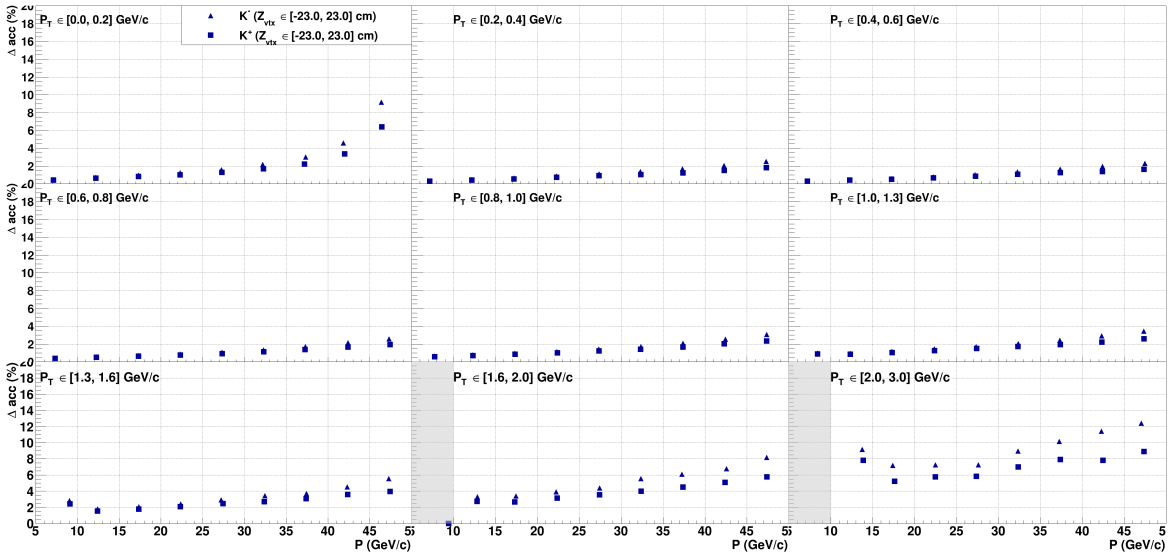

(b) $Z_{vtx} \in [-23, 23]$ cm

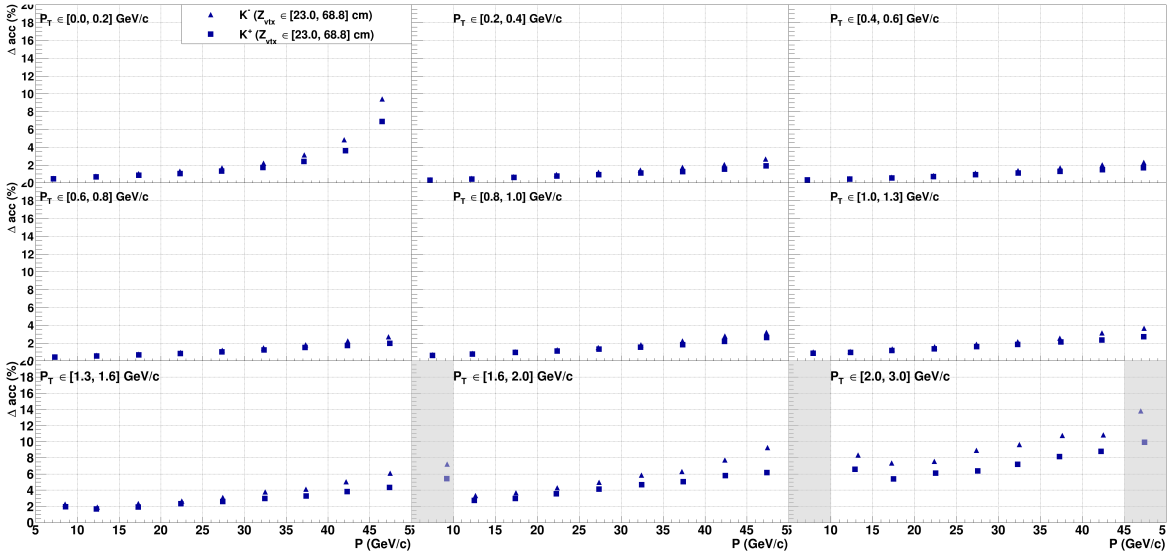

(c) $Z_{vtx} \in [23, 68]$ cm

Figure 4.9: Distributions of **acceptance relative error** for the different Z_{vtx} bins for **kaons** as a function of momentum in bins of transverse momentum. The two different charges are also plotted together.

Plots in figure 4.10 show the acceptance corrections for kaons. From this figure, we can conclude that the same behavior observed in acceptance corrections for pions is also present in kaons. The acceptance drops with momentum and rises with transverse momentum, and a dependence in Z_{vtx} is observed as well. In the bins $P \in [5,10]$ GeV/c, the acceptance is significantly lower when compared to the others; this is likely an effect of the RICH-1 kaon identification threshold mentioned before.

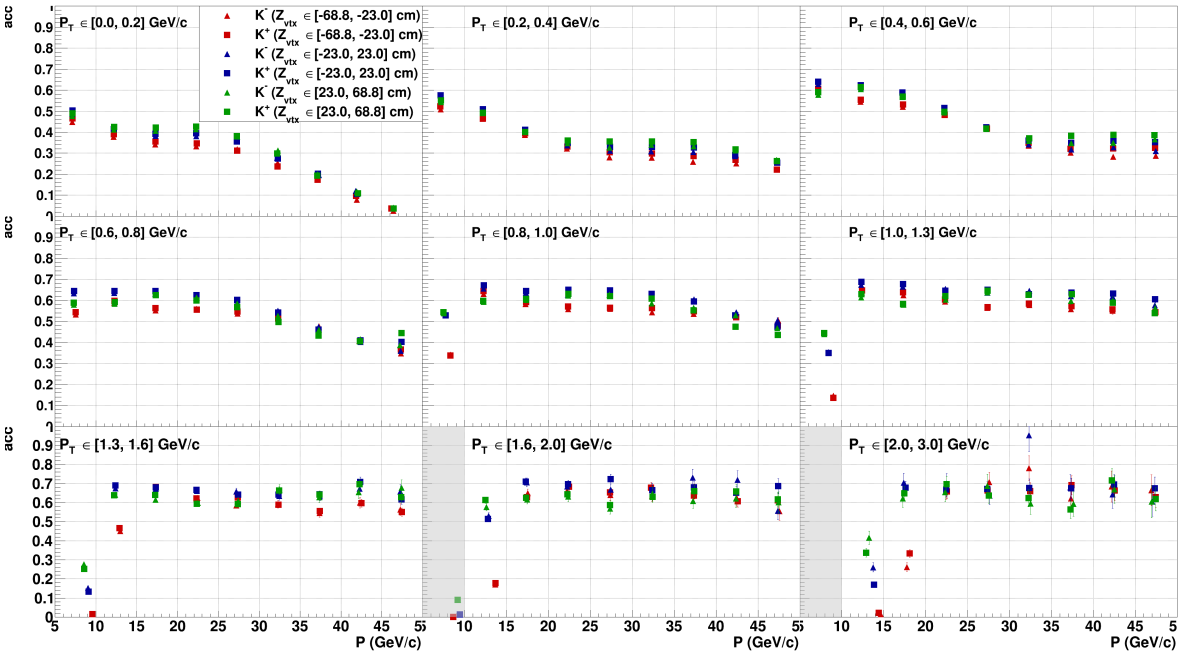

Figure 4.10: **Acceptance** corrections for **kaons** as a function of momentum in bins of transverse momentum and Z_{vtx}.

4.4.2.3 Protons

The relative error of the acceptance corrections for the proton and antiproton is plotted in Figure 4.11. The first two momentum bins, $P \in [5,10]$ GeV/c and $P \in [10,15]$ GeV/c, will be discarded because of the RICH-1 identification threshold (18 GeV/c). For 4.11a and 4.11b, the bin $P_t \in [0.0,0.2]$ GeV/c, $P \in [45,50]$ GeV/c doesn't have more than 100 entries, so will also be discarded. For $P_t \in [0.0,0.2]$ GeV/c in all of the canvases, all the momentum bins have less than or slightly above 100 entries, so this entire transverse momentum range will not be selected.

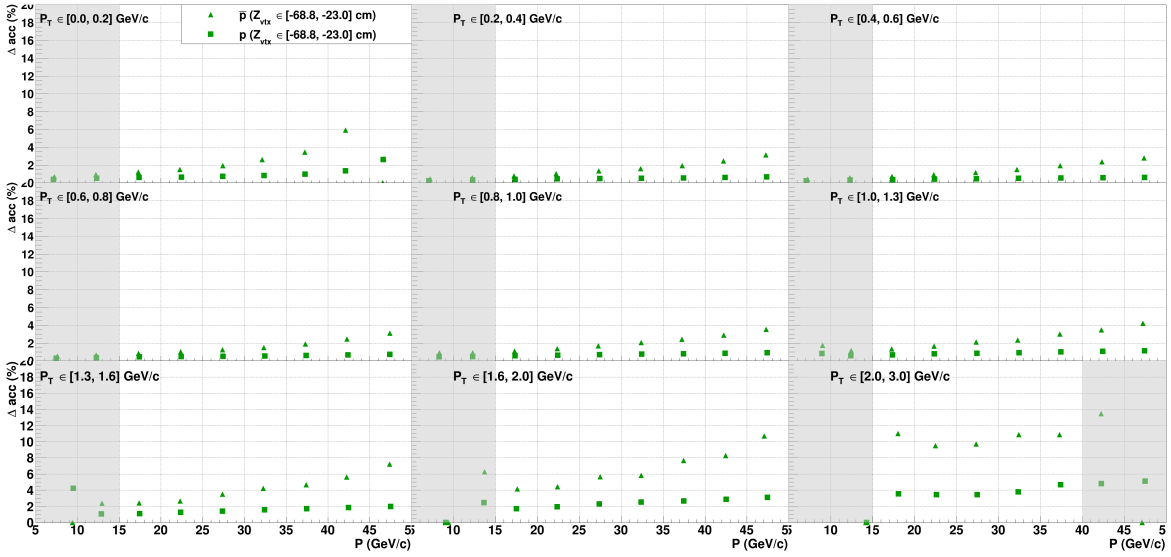

(a) $Z_{vtx} \in [-68, -23]$ cm

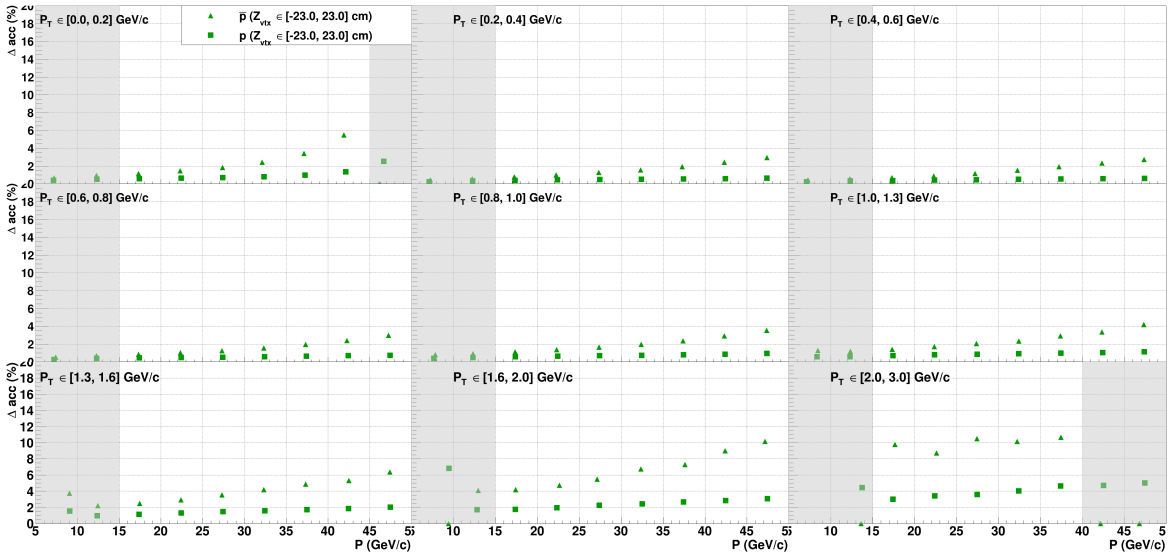

(b) $Z_{vtx} \in [-23, 23]$ cm

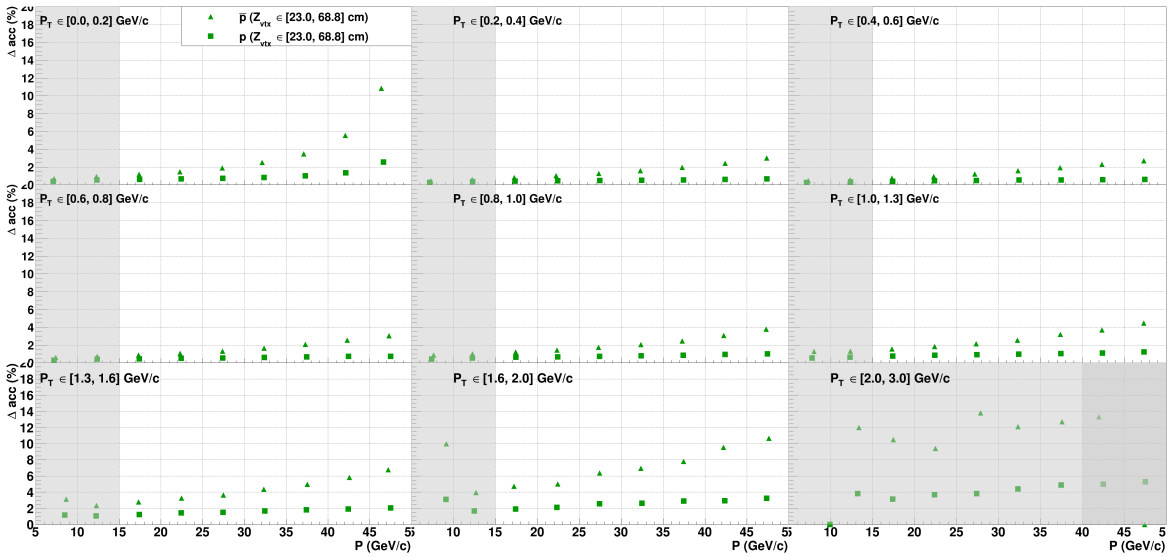

(c) $Z_{vtx} \in [23, 68]$ cm

Figure 4.11: Distributions of **acceptance relative error** for the different Z_{vtx} bins for **protons** and **antiprotons** as a function of momentum in bins of transverse momentum. The two different charges are also plotted together.

Figure 4.12 shows the acceptance corrections for protons/antiprotons. The acceptance values do not decrease as sharply with momentum as it was observed for the pions and kaons. However, it seems that the number of entries sharply decreases with P_t, which is demonstrated by the size of the error bars. This is likely because protons are the heaviest of the three hadrons and have a less pronounced curve in the spectrometer, when crossing the magnetic field of the SM1 dipole magnet.

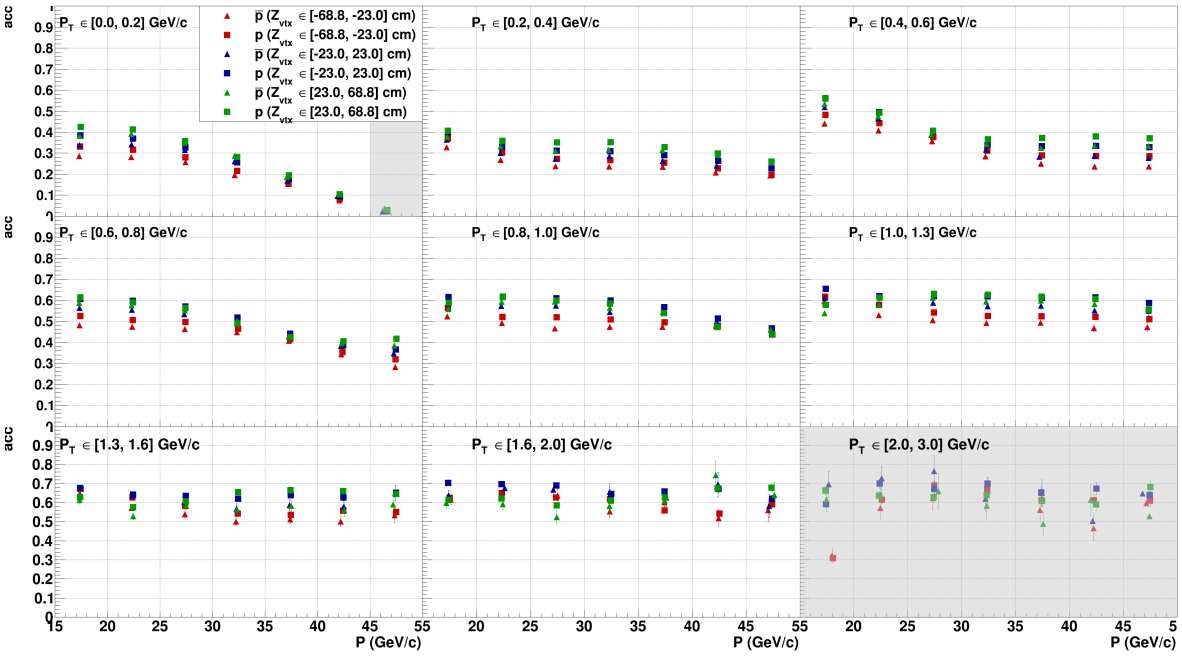

Figure 4.12: **Acceptance** corrections for **protons** and **antiprotons** as a function of momentum in bins of transverse momentum and Z_{vtx}.

Chapter 5

Cross-section ratios

To calculate the cross section, there are several important ingredients that need to be accounted for. The formula, for each hadron, is given by:

$$\sigma^h = \frac{N^h_{true}}{\mathscr{L} \cdot acc} \tag{5.1}$$

- N^h_{true} - Number of events for a determined bin after accounting for the particle h identification efficiency.
- acc - Acceptance as a convolution of geometrical acceptance, efficiency of reconstruction, and trigger efficiency.
- $\mathscr{L}$ - Luminosity, which depends on the beam intensity and the number of interaction centers in the target.

In chapter 3, we determined the number of events identified; chapter 4 was dedicated to calculating the acceptance; the luminosity will not be calculated due to it being equal for the productions of positive and negative hadrons. The goal of this chapter is to calculate the true number of events in each bin by applying corrections from the RICH identification efficiencies, which we call RICH unfolding, and to calculate the final cross-section ratios.

5.1 RICH-1 unfolding

As previously observed, although the RICH-1 detector has a high efficiency of identification, there are still some bad reconstruction effects, such as population contamination. For this reason, the RICH unfolding matrix will be used to calculate the true number of each type of hadrons in each bin. The RICH matrix is divided into bins of momentum and polar angle, and for each bin, we have a 3×3 matrix such as:

$$M^{+/-}(p,\theta) = \begin{pmatrix} \varepsilon(\pi \to \pi) & \varepsilon(K \to \pi) & \varepsilon(p \to \pi) \\ \varepsilon(\pi \to K) & \varepsilon(K \to K) & \varepsilon(p \to K) \\ \varepsilon(\pi \to p) & \varepsilon(K \to p) & \varepsilon(p \to p) \end{pmatrix} \tag{5.2}$$

where each entry in the diagonal $\varepsilon(i \to i)$ represents the efficiency of identification for the particle i, and each off-diagonal entry $\varepsilon(i \to j)$ represents the probability of particle i being mis-identified by particle j. Thus, two vectors were considered, N^h_{id} and N^h_{true}, which respectively correspond to the number of

RICH-identified hadrons and the number of true-type hadrons in each bin. Finally, for each charge, the unfolding is given by:

$$N^h_{true} = M^{-1} N^h_{id} \tag{5.3}$$

The RICH-1 PID efficiency matrix was obtained beforehand by Giordano D. in [8] from the decay channels of secondary vertices (V0): $K^0_s \to \pi^+\pi^-$, $\Lambda \to \pi^- p$ and $\bar{Lambda} \to \pi^+ \bar{p}$, and the Armenteros-Podolanski plot to determine the efficiency with which the RICH correctly identifies charged pions, kaons, proton and antiproton. The RICH matrix was defined for $P \in [10, 60]$ GeV/c and $\theta \in [0.01, 0.18]$ rad ranges. Consequently, the hadron spectra momentum range had to be reduced to $P \in [10, 50]$ GeV/c.

The hadron spectra histograms were filled with the unfolding and acceptance corrections as event-weights, so the plots shown in this section have acceptance corrections already applied.

5.1.1 Pions

Figure 5.1 plots the pion unfolded spectra with acceptance and RICH unfolding. This plot gives us the production cross sections of these particles in arbitrary units, due to the lack of luminosity corrections. We can observe from this figure that production of matter is greater when compared to production of antimatter, as expected, so it will also be expected that the cross-section ratios antimatter/matter are below 1.

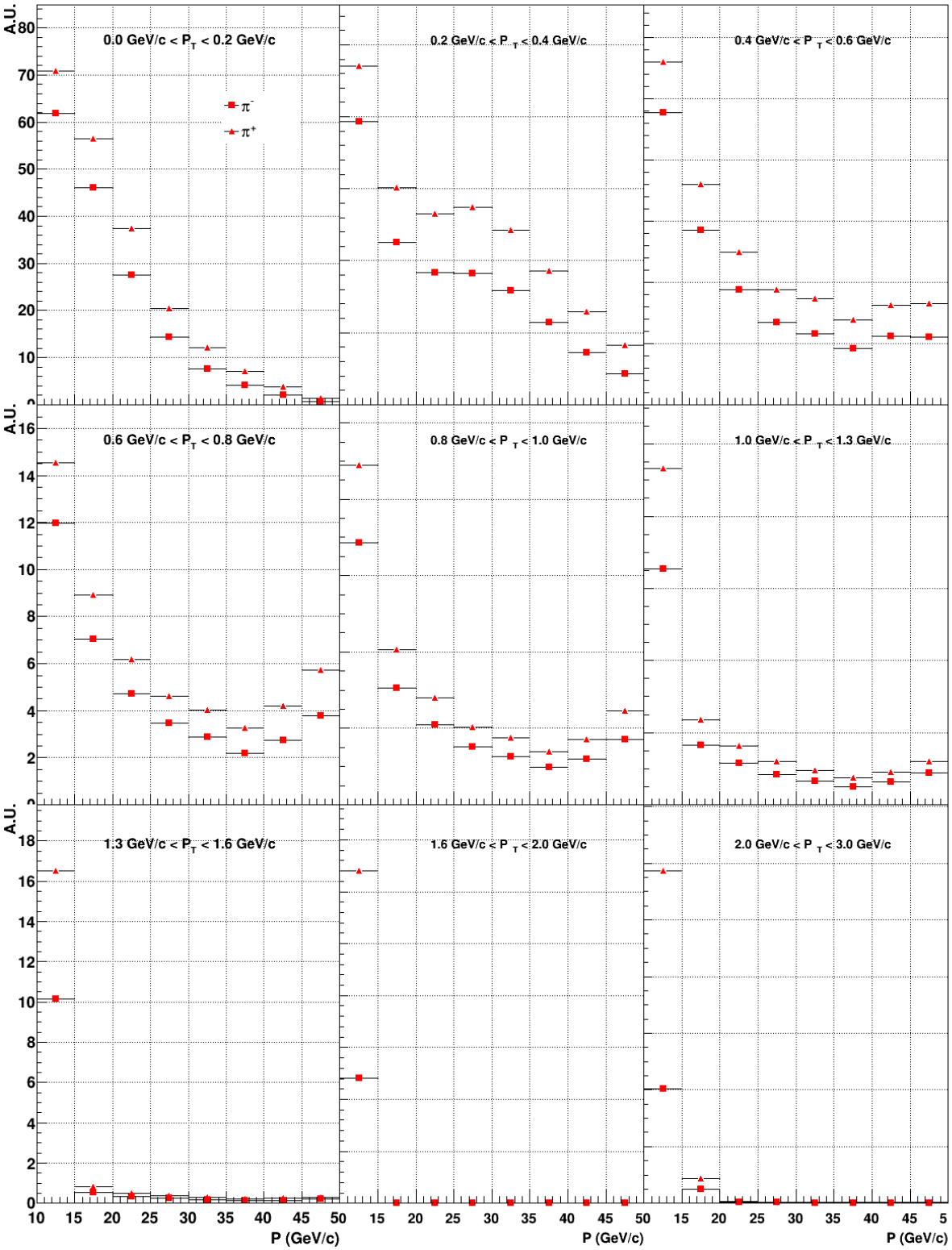

Figure 5.1: Spectra for pions with acceptance and RICH unfolding applied.

5.1.2 Kaons

The cross sections for positive and negative kaons are plotted in Figure 5.2. These distributions show a greater separation between the two charges, particularly in larger P_t.

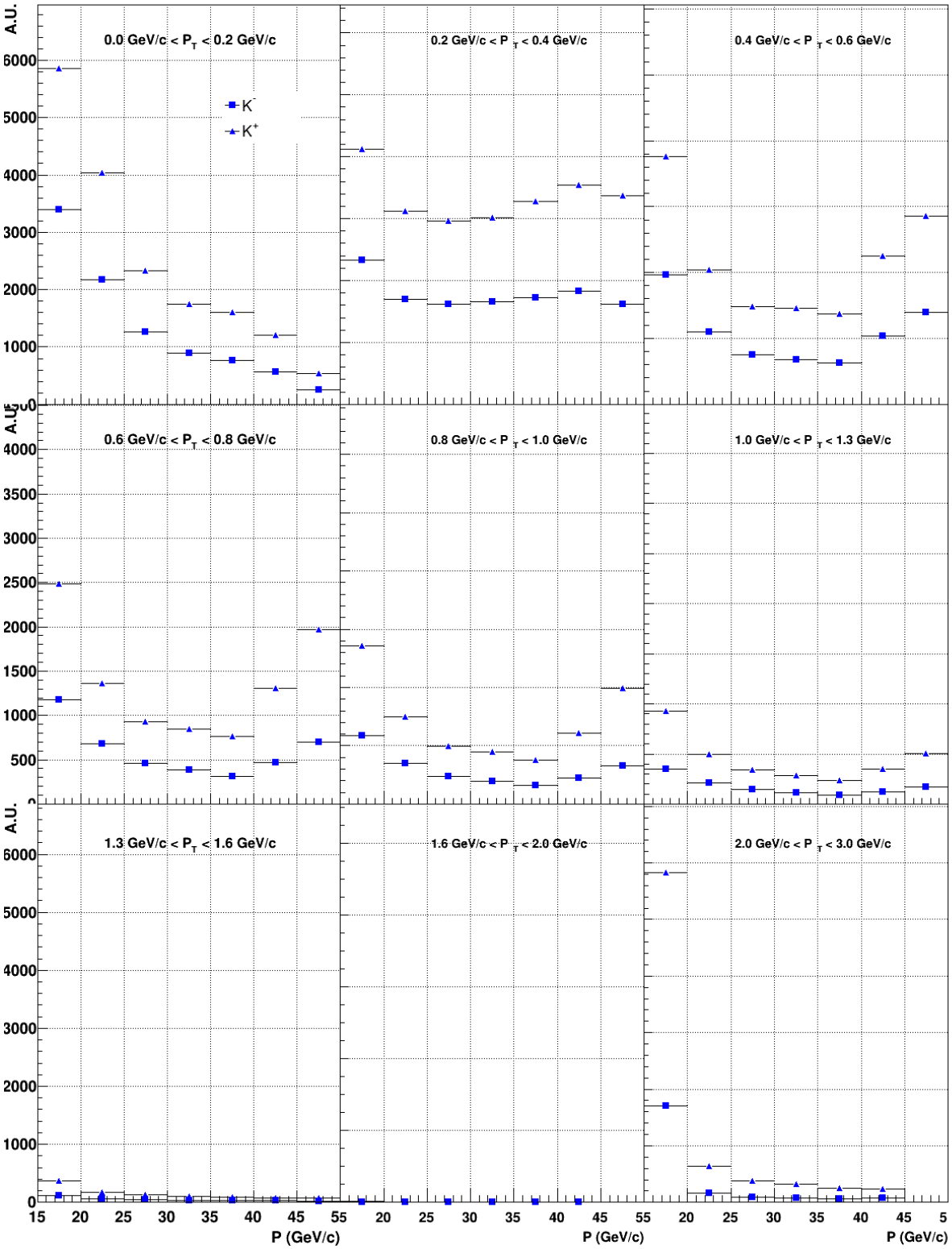

Figure 5.2: Spectra for kaons with acceptance and RICH unfolding applied.

5.1.3 Protons

We can observe from the production cross section of protons and antiprotons plotted in figure 5.3 that the first bin of momentum, $P \in [15, 20]$ GeV/c, usually has fewer entries than the rest due to the RICH-1

identification threshold of $P > 17$ GeV/c , i.e. in this bin the assumption that the particle identification efficiency is 100% is clearly overestimated (but affects protons and antiprotons in roughly the same way). We can also observe that, as was the case with pions and kaons, the production of antiprotons is much less compared to the production of protons.

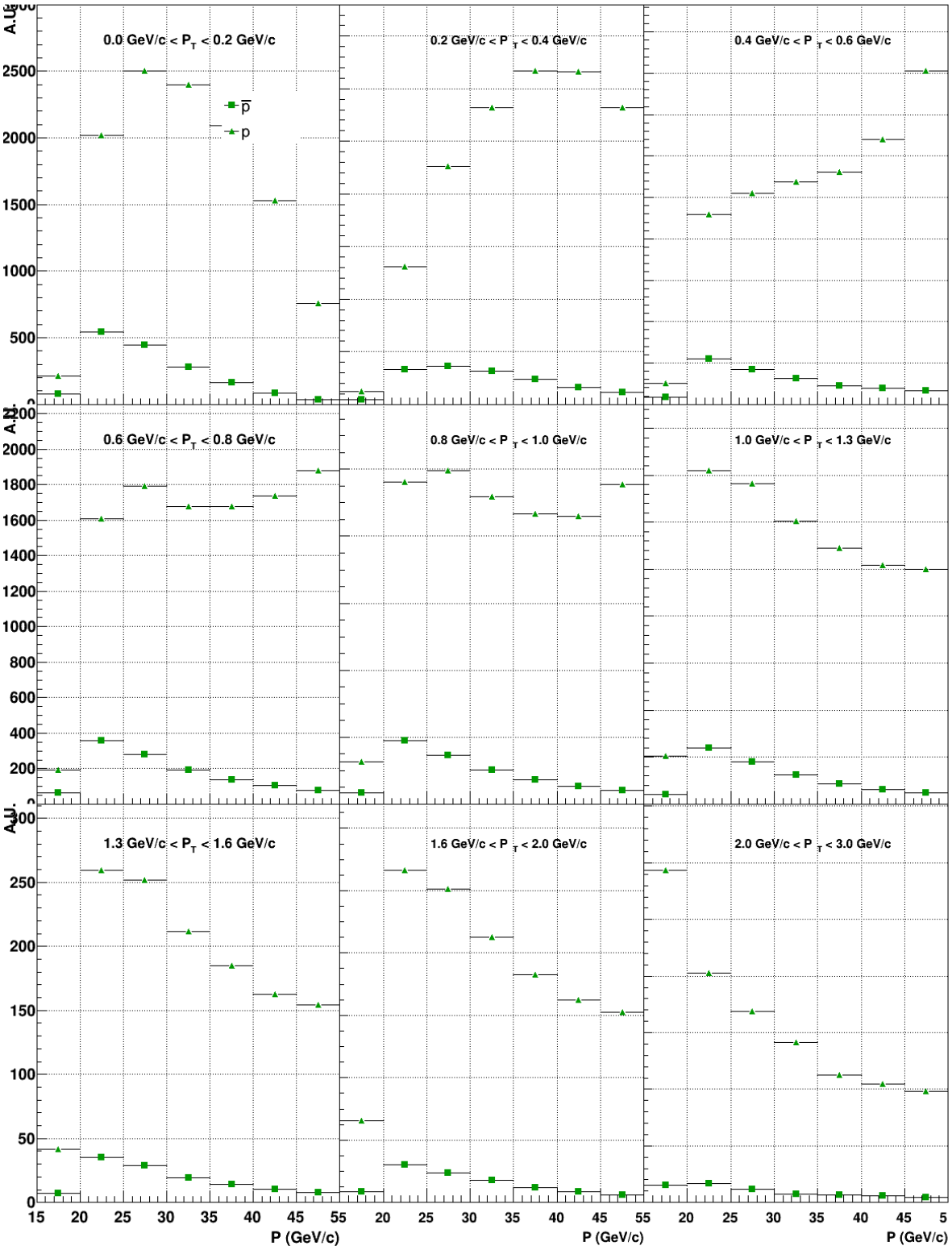

Figure 5.3: Spectra for protons/antiprotons with acceptance and RICH unfolding applied.

5.2 Cross-section ratios

Figures 5.4, 5.5, and 5.6 show the comparisons between each negative hadron cross section and its respective positive counterpart. These figures also show which bins were rejected based on the criteria described in chapter 4 in gray shading. The statistical error bars are also displayed; however, they are too small to be noticeable.

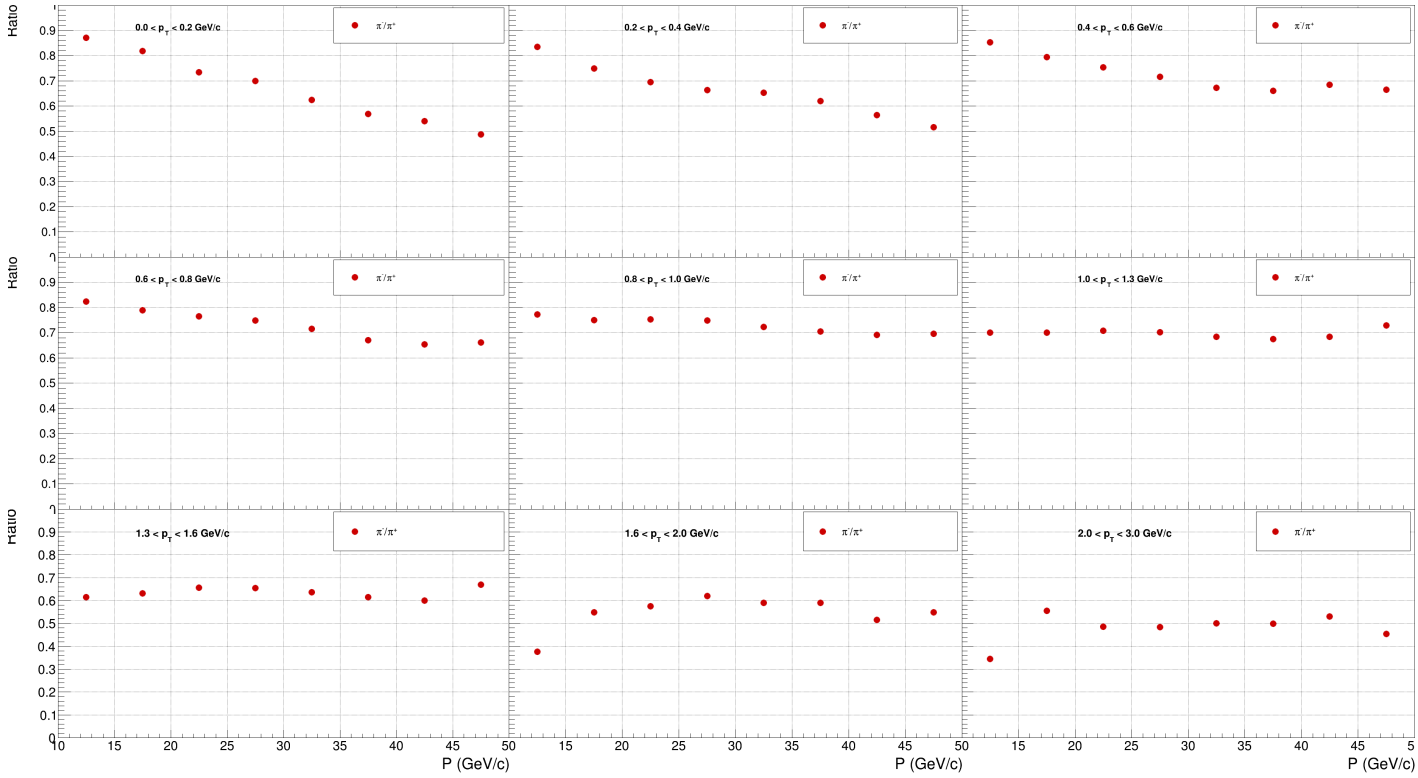

Figure 5.4: Cross-section ratios for pions as a function of momentum. Each pad represents a bin of transverse momentum.

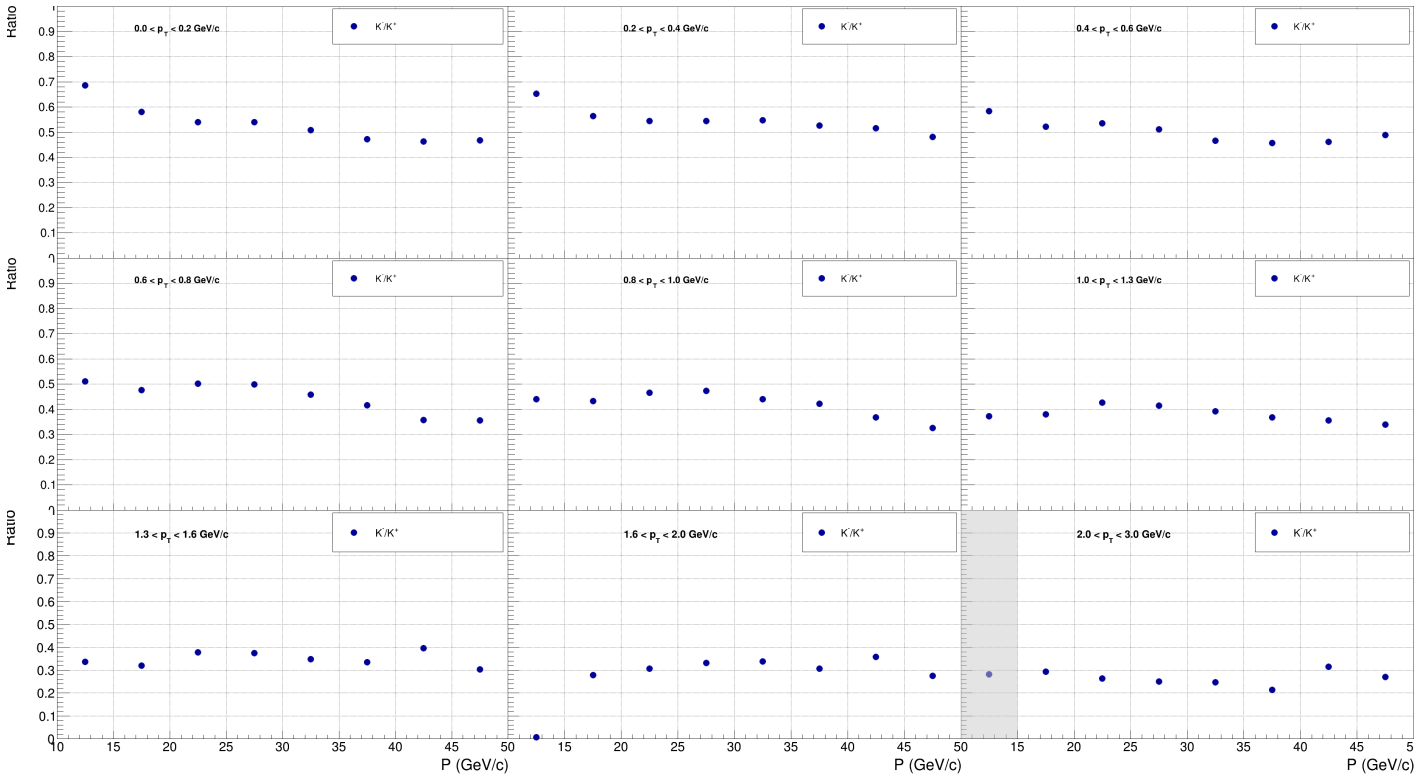

Figure 5.5: Cross-section ratios for kaons as a function of momentum. Each pad represents a bin os transverse momentum.

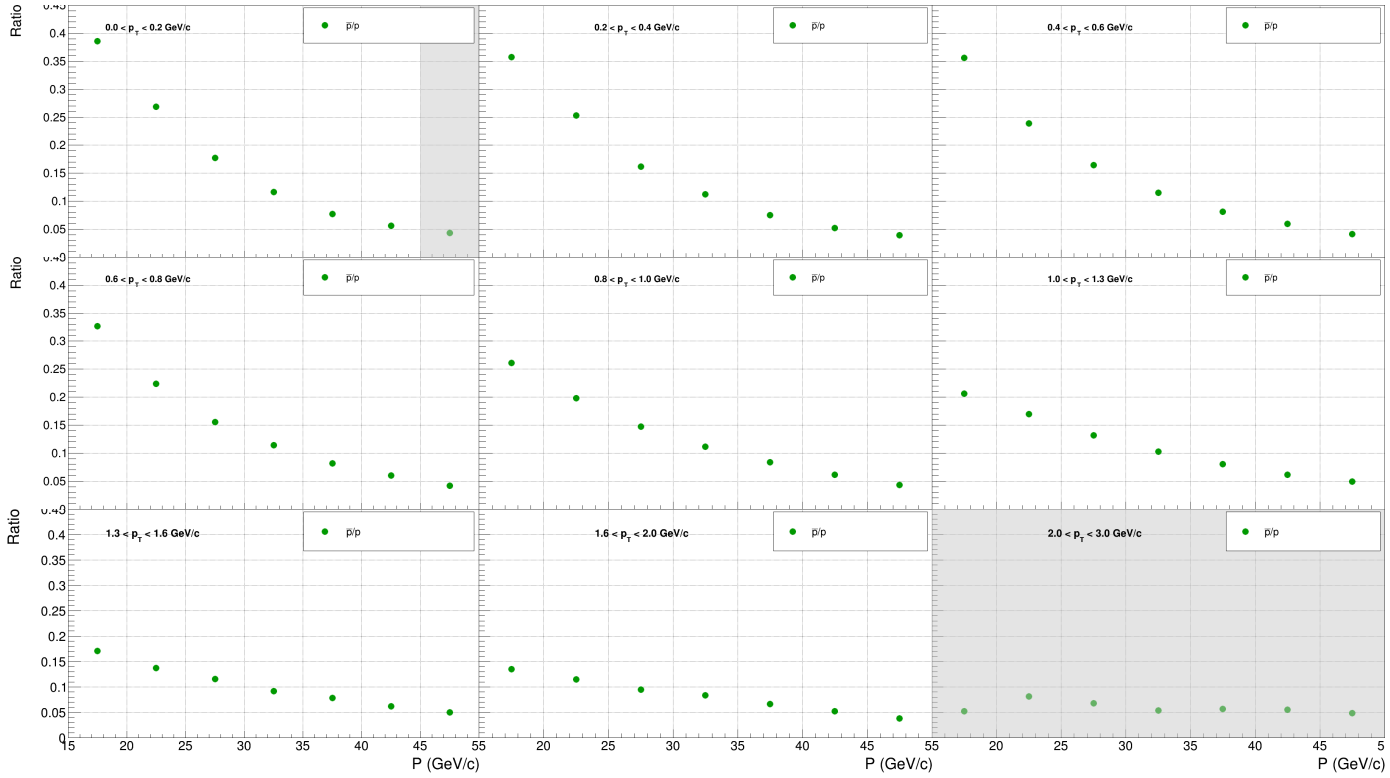

Figure 5.6: Cross-section ratios for antiprotons/protons as a function of momentum. Each pad represents a bin os transverse momentum. Bins that were previously rejected are shaded in gray.

Chapter 6

Conclusions

Dark matter is invisible but may leave traces through cosmic-ray standard model particles (like antiprotons). Current uncertainties in proton–proton and proton–helium cross-sections limit how well we can model cosmic-ray antiproton production. The AMBER experiment at CERN measures these processes directly with high precision. In this thesis, we set out to determine the cross-sections of hadrons with < 3% uncertainty, improving input for dark matter studies.

The final results for the antiproton-to-proton cross-section ratios were successfully calculated. These values were also previously calculated for different track and event selection criteria and a different Monte Carlo simulation in [8]. We observe that the values calculated in this thesis approximately match the ones obtained in [8] with slight variations.

The only type of error calculated in this thesis is the statistical error, which has a maximum value of approximately 1.0% for pions, 1.8% for kaons, and 2.0% for protons/antiprotons. However, there are other sources of error, particularly the systematic errors. Such sources are:

- The error associated with the RICH unfolding matrix in the process of outgoing hadron identification.
- The error associated with the beam proton identification.
- Acceptance calculations. As seen in 4, the Monte Carlo simulation does not accurately represent reality, leading to errors in the acceptance calculations.
- The bad time calibrations observed in 3 could also lead to reconstructing tracks to the wrong vertices.
- The high mean value of the χ^2/ndf of outgoing tracks is also higher than the desired value. This could lead to errors in final calculations.

In further work, sources of systematic error should be accounted for in order to obtain the cross-section ratios with total uncertainty below 3%. As it was observed in chapter 3, a new production should be obtained to fix the problems with time reconstruction in the MP01 detector. After the analysis is completed for this period, the same study should be performed for other periods corresponding to different beam energies.

Bibliography

[1] D.-Y. Chung et al., "A unifying theory of dark energy, dark matter, and baryonic matter in the positive-negative mass universe pair: Protogalaxy and galaxy evolutions", *Journal of Modern Physics*, vol. 11, no. 07, p. 1091, 2020.

[2] M. Korsmeier, F. Donato, and M. Di Mauro, "Production cross sections of cosmic antiprotons in the light of new data from the NA61 and LHCb experiments", *Phys. Rev. D*, vol. 97, p. 103 019, 10 May 2018. DOI: 10.1103/PhysRevD.97.103019. [Online]. Available: https://link.aps.org/doi/10.1103/PhysRevD.97.103019.

[3] B. Adams et al., "A new QCD facility at the M2 beam line of the cern sps: COMPASS++/AMBER", Tech. Rep., 2019.

[4] M. Kachelriess, I. V. Moskalenko, and S. S. Ostapchenko, "New calculation of antiproton production by cosmic ray protons and nuclei", *The Astrophysical Journal*, vol. 803, no. 2, p. 54, Apr. 2015. DOI: 10.1088/0004-637X/803/2/54. [Online]. Available: https://doi.org/10.1088/0004-637X/803/2/54.

[5] G. Graziani et al., "Fixed target physics at LHCb", *Int. J. Mod. Phys. A30*, p. 1 530 022, 2015.

[6] D. Maurin et al., "Precision cross-sections for advancing cosmic-ray physics and other applications: A comprehensive programme for the next decade", *unpublished*, 2025. DOI: https://doi.org/10.48550/arXiv.2503.16173.

[7] P. Abbon et al., "The COMPASS experiment at CERN", *Nuclear Instruments and Methods in Physics Research Section A: Accelerators, Spectrometers, Detectors and Associated Equipment*, vol. 577, no. 3, pp. 455–518, 2007, ISSN: 0168-9002. DOI: https://doi.org/10.1016/j.nima.2007.03.026. [Online]. Available: https://www.sciencedirect.com/science/article/pii/S0168900207005001.

[8] D. Giordano, "Antiproton production measurement for indirect Dark Matter search at the AMBER experiment at CERN", Ph.D. dissertation, Università degli Studi di Torino, Italy, 2024.

[9] P. Abbon et al., "The COMPASS setup for physics with hadron beams", *Nuclear Instruments and Methods in Physics Research Section A: Accelerators, Spectrometers, Detectors and Associated Equipment*, vol. 779, pp. 69–115, 2015, ISSN: 0168-9002. DOI: https://doi.org/10.1016/j.nima.2015.01.035. [Online]. Available: https://www.sciencedirect.com/science/article/pii/S0168900215000662.

[10] C. Bovet, R. Maleyran, L. Piemontese, A. Placci, M. Placidi, et al., "The cedar counters for particle identification in the sps secondary beams: A description and an operation manual", European Organization for Nuclear Research, Geneva (Switzerland), Tech. Rep., 1982.

[11] C. Bierlich et al., "A comprehensive guide to the physics and usage of PYTHIA 8.3", *SciPost Phys. Codebases*, vol. 8, 2022.

BIBLIOGRAPHY

[12] S. Agostinelli et al., “Geant4 – a simulation toolkit”, *Nucl. Instrum. Meth. A*, vol. 506, pp. 250–303, 2003).